

1 A comparison of Eulerian and Lagrangian transport and
2 non-linear reaction algorithms

3 David A. Benson

4 *Hydrological Science and Engineering, Colorado School of Mines, Golden, CO, 80401,*
5 *USA. (dbenson@mines.edu)*

6 Tomás Aquino and Diogo Bolster

7 *Civil and Environmental Engineering, University of Notre Dame, Notre Dame, IN,*
8 *46556, USA. (tomas.c.aquino@gmail.com, dbolster@nd.edu)*

9 Nicholas Engdahl

10 *Civil and Environmental Engineering, Washington State University, Pullman WA 99164,*
11 *USA. (nick.engdahl@wsu.edu)*

12 Christopher V. Henri and Daniel Fernández-García

13 *Department of Geotechnical Engineering and Geosciences, Universitat Politècnica de*
14 *Catalunya, Barcelona, Spain (christopher.henri@upc.edu, daniel.fernandez.g@upc.edu)*

15 **Abstract**

16 Chemical reaction rates measured in field aquifers are typically much lower
17 than those measured in the laboratory, primarily due to poorer mixing of
18 chemically distinct waters at the larger scale. As a result, realistic field-scale
19 predictions require accurate simulation of the degree of mixing between flu-
20 ids. The Lagrangian particle-tracking (PT) method is a now-standard way
21 to simulate the transport of conservative or sorbing solutes. The method's
22 main advantage is the absence of numerical dispersion (and its artificial mix-
23 ing) when simulating advection. New algorithms allow particles of differ-
24 ent species to interact in nonlinear (e.g., bimolecular) reactions. Therefore,
25 the PT methods hold a promise of more accurate field-scale simulation of
26 reactive transport because they eliminate the masking effects of spurious
27 mixing due to advection errors inherent in grid-based methods. A hypothet-
28 ical field-scale reaction scenario is constructed and run in PT and Eulerian
29 (finite-volume/finite-difference) simulators. Grid-based advection schemes

30 considered here include 1st- to 3rd-order spatially accurate total-variation-
31 diminishing flux-limiting schemes, both of which are widely used in current
32 transport/reaction codes. A homogeneous velocity field in which the Courant
33 number is everywhere unity, so that the chosen Eulerian methods incur no
34 advection error, shows that both the Eulerian and PT methods can achieve
35 convergence in the L^1 (integrated concentration) norm, but neither shows
36 stricter pointwise convergence. In this specific case with a constant disper-
37 sion coefficient and bimolecular reaction $A+B \rightarrow P$, the correct total amount
38 of product is $0.221M_{A0}$, where M_{A0} is the original mass of reactant A . When
39 the Courant number drops, the grid-based simulations can show remarkable
40 errors due to spurious over- and under-mixing. In a heterogeneous velocity
41 field (keeping the same constant and isotropic dispersion), the PT simula-
42 tions show an increased reaction total from $0.221M_{A0}$ to $0.372M_{A0}$ due to
43 fluid deformation, while the 1st-order Eulerian simulations using $\approx 10^6$ cells
44 (with a classical grid Peclet number $\Delta x/\alpha_L$ of 10) have total product of
45 $0.53M_{A0}$, or approximately twice as much additional reaction due to advec-
46 tion error. The 3rd-order TVD algorithm fares better, with total product of
47 $0.394M_{A0}$, or about 1.14 times the increased reaction total. A very strict
48 requirement on grid Peclet numbers for Eulerian simulations will be required
49 for realistic reactions because of their nonlinear nature. We analytically es-
50 timate the magnitude of the effect for the end-member cases of very fast
51 and very slow reactions. For the bimolecular reaction studied here, the com-
52 putational demands of the particle-killing methods are much smaller than,
53 and the particle-number-preserving algorithm are on par with, the fastest
54 Eulerian methods.

55 *Keywords:* Particle tracking, Chemical reaction, Numerical dispersion,
56 Nonlinear amplification

57 *PACS:* 02.50.Ey, 02.50.Ga, 02.70.Ns, 05.10.Gg

58 1. Introduction

59 Chemical reactions occur ubiquitously at a multitude of scales in hy-
60 drologic and hydrogeologic environments. A common observation is that
61 reactions progress at lower rates at larger scales. Imperfect mixing is an im-
62 portant contributor to the various processes that contribute to the scaling
63 of reaction rates [38]. Mixing is the fundamental process that brings reac-
64 tants into contact with one another and accurate simulations of mixing are

65 key to correctly predicting reactions [36, 37, 47]. Recent studies of mixing
66 in heterogeneous hydrologic systems demonstrate that complex rate changes
67 can emerge, and simple assumptions about upscaled rates have been shown
68 to lack realism [62, 61, 63, 24, 19, 21]. While most of these studies have
69 focused on mixing of conservative solutes (and/or instantaneous reactions),
70 the results have broad implications for all mixing-driven and rate-limited re-
71 actions [36, 37, 24]. Many numerical and experimental studies have shown
72 that governing equations or numerical models that do not adequately simu-
73 late mixing will also suffer error in ultimately predicting chemical reactions
74 [47, 33, 32, 39, 87, 80].

75 Many numerical approaches exist for modeling transport of *non-reactive*
76 solutes through heterogeneous porous media. A recent paper [20] focuses
77 on five currently popular schemes. Broadly speaking, these authors con-
78 clude that, because of spurious numerical dispersion, the grid-based Eulerian
79 schemes overestimate dilution/mixing, while Lagrangian approaches, includ-
80 ing both random walk particle tracking (RWPT) and Smoothed Particle
81 Hydrodynamics (SPH) approaches, given a sufficiently resolved and smooth
82 velocity field, are free of numerical dispersion. The authors report that
83 SPH is relatively computationally demanding and does not readily han-
84 dle anisotropic dispersion [3]. Furthermore, the discrete nature of RWPT
85 can lead to discontinuous concentrations, although a variety of novel algo-
86 rithms have evolved in recent years to remove such spurious fluctuations
87 [44, 78]. While the errors associated with these methods for non-reactive
88 solutes are well known, the complicating factor of nonlinear reactions (which
89 may amplify these errors), has been recognized but only qualitatively re-
90 ported [27]. In this paper, we take a more quantitative look at the difference
91 between several widely-used Eulerian (grid-based) and Lagrangian reactive
92 transport algorithms. For reactive transport, grid-based methods—including
93 finite-element, finite-volume, and finite-difference—continue to largely be the
94 norm, although there have been significant recent advances in Lagrangian ap-
95 proaches [11, 94, 95, 42, 18]. Here we will focus on classical finite-volume/finite-
96 difference Eulerian methods and the purely Lagrangian PT advection-dispersion-
97 reaction schemes.

98 Regarding the widespread use of grid-based codes, we highlight a few ap-
99 proaches and recent studies. More detailed descriptions are given by Steefel
100 et al. [91]. While different in their underlying numerical method (finite-
101 volume, finite-element, integrated finite-difference, etc.), PFLOTRAN [69],
102 TOUGHREACT [106], HYDROGEOCHEM [107], FEHM [110] and NUFT

103 [74] use a 1st-order spatially accurate ($\mathcal{O}(\Delta x)$) upwind advection scheme (al-
 104 though NUFT allows an iterative scheme to improve accuracy [89]). The
 105 TOUGH and TOUGHREACT family of codes is routinely used to simulate
 106 CO₂ injection and reaction [e.g., 75, 2]. Hammond and Lichtner [48] use
 107 PFLOTRAN to simulate Uranium transport and speciation on the several-
 108 kilometer scale. Navarre-Sitchler et al. [73] use PFLOTRAN, and Keating
 109 et al. [56] use FEHM to simulate the release of metals and Uranium, respec-
 110 tively, from CO₂-acidified aquifers. None of these studies specify values for
 111 dispersivity or diffusivity, so it is likely that the authors rely on numerical
 112 error, which is a function of discretization and local velocity, to emulate real
 113 dispersion. Regardless of which code is selected, the effects of realistic disper-
 114 sion on reaction are often ignored and the fastest and least accurate transport
 115 algorithm is used [55]. Steefel [90] and White and Oostrom [104] recognize
 116 the importance of spurious dispersion and mixing (particularly transverse to
 117 flow) on reactions and implement a 2nd-order accurate variant of Leonard’s
 118 [65, 31] 3rd-order total-variation-diminishing (TVD) scheme. However, these
 119 codes use a 1st-order upwind scheme when the simultaneous implicit reaction
 120 and transport option is chosen. Finally, reaction algorithms (i.e., PHT3D
 121 [6, 82]) based on transport in the MT3DMS code [109] may choose among
 122 several advection schemes including 1st and 3rd-order ($\mathcal{O}(\Delta x^3)$) TVD algo-
 123 rithms. One may also choose a mixed Lagrangian/Eulerian scheme in which
 124 advection is performed by particles and dispersion/reaction are performed
 125 on a grid after mapping particle masses back into gridded concentrations
 126 similar to the scheme by Tompson and Dougherty [97]. It is notable that
 127 Prommer et al. [82] compare the strictly Eulerian methods to the hybrid La-
 128 grangian/Eulerian advection/dispersion scheme in MT3DMS and find that
 129 this Lagrangian/Eulerian scheme is superior to the 3rd-order Eulerian scheme
 130 in MT3DMS. Those authors recommend the use of particle-tracking for ad-
 131 vection as a general rule, and a similar conclusion was reached by Herrera
 132 et al. [51] with their SPH model.

133 While more accurate (higher order) grid-based advection schemes have
 134 been developed (see, e.g., [98]), including the weighted essentially non-oscillatory
 135 (WENO) and advection-diffusion-reaction (ADER) families of methods, they
 136 have not been widely adopted in studies of aquifer geochemical reactions.
 137 One possible reason is the relatively complex nature of these methods, which
 138 reconstruct (interpolate) the profiles of the advected quantities using n^{th} -
 139 order polynomials. The polynomials can be analytically advected with $(n +$
 140 $1)^{\text{th}}$ -order accuracy in 1- d , but the construction process is somewhat compli-

141 cated and a matter of choice. Moving the methods to multi-dimensions is also
142 tricky, because maintaining high-order accuracy requires an algorithm that
143 looks in all directions (not simply a combination of 1-D sweeps) [98, 68, 67].
144 The higher-order polynomial reconstruction can be extended to arbitrary-
145 order polynomial basis functions in finite-element implementations [28, 70, 4]
146 with analogous results to the WENO finite volume algorithms [e.g., 59]. A
147 further complication to many higher-order methods is the potential for neg-
148 ative concentration oscillations and/or mass balance errors when spurious
149 negative masses are quashed. Another method used to increase accuracy
150 uses adaptive grid refinement to decrease grid size in areas of large concen-
151 tration gradients (e.g., [105, 30, 72]). These and other efforts to improve
152 the efficiency, accuracy, and parallel implementation of Eulerian methods for
153 advective flux continue [e.g., 57, 53]. But the situation remains that 1st-
154 through 3rd- order accurate, directionally split, upstream weighting is the
155 prevailing solution method in aquifer transport and reaction studies; there-
156 fore, we investigate these schemes.

157 One issue with the various Eulerian implementations is that artificial mix-
158 ing is exacerbated by low Courant numbers (low velocities). As a result, the
159 artificial dispersion in the transverse, low-velocity direction can be as great as
160 either the spurious or real dispersion in the longitudinal direction. This spu-
161 rious transverse mixing is responsible for overestimating reactions for many
162 boundary value problems [27]. To address this problem, *Cirpka et al.* [27]
163 developed a gridding-along-streamlines approach. In 2-*d* the streamlines can
164 be solved analytically, but in 3-*d*, particles must be used to trace streamlines
165 or streamtubes in the areas of interest. The domain is re-discretized along
166 streamlines so that advective fluxes do not cross cells in the transverse direc-
167 tion. Solving dispersion and reaction is then either done on the Eulerian grid,
168 or the particles used to trace streamlines can be treated via SPH kernels, and
169 the problem is reduced to minimizing error in the longitudinal direction. In
170 complex flows, however, excess longitudinal dispersion can deplete reactants
171 that are rotated and placed into lateral contact, so depending on the configu-
172 ration of reactants, longitudinal errors in one location can influence reaction
173 errors in another (see, e.g., [35, 64, 43]).

174 The various issues with purely Eulerian and mixed Lagrangian/Eulerian
175 methods motivated the development of purely Lagrangian transport and re-
176 action algorithms. The Lagrangian particle-tracking (PT) method for simu-
177 lating *passive scalar* transport has several features that have justified their
178 continued development and implementation [60, 85, 9]. These include 1)

179 independence of the simulation speed from the underlying velocity (and hy-
180 draulic conductivity) discretization, 2) computationally simple representa-
181 tion of temporal [12, 84] and/or spatial nonlocality [108], and 3) the lack of
182 artificial mixing and negative concentrations. The PT method was extended
183 to simulate chemical reactions by calculating the physically-based probabilit-
184 ity of particle collision and subsequent conditional probability of reaction
185 [11, 18]. In this framework, the chemical reactions occur without an explicit
186 calculation of concentrations, thus removing the need for interpolation onto
187 an Eulerian grid or using SPH kernels for dispersion and reaction calculation
188 [e.g. 97, 81, 3], which can reintroduce numerical dispersion and other inter-
189 polation errors. Instead, the proximity of particles in the flow field dictate
190 the occurrence of reactions. This point highlights a potential advantage of
191 the PT method over Eulerian reactive transport models because imperfect
192 mixing and chemical spatial heterogeneity are represented by particle num-
193 bers and proximities at all scales [76, 77], whereas perfect mixing is assumed
194 at some scale in grid-based models. Furthermore, this PT reaction algorithm
195 can be derived and applied to experimental data without the need for em-
196 pirical parameters such as effective reaction radii or rates, providing a direct
197 link to the physical mechanics of chemical reactions [39].

198 One of the goals of the work on PT methods is to provide a theoret-
199 ical basis for upscaling effective reaction rates in heterogeneous flow fields
200 within larger-scale Eulerian codes, based on subgrid fluid deformation met-
201 rics [35, 43]. When an incompressible fluid moves through porous media, the
202 velocity field influences reactions by deforming a hypothetical fluid parcel.
203 Gradients in the velocity field will cause stretching of the fluid parcel in one
204 dimension which is accompanied by compression in others. Compression can
205 bring fluids of different composition into closer proximity, facilitating mix-
206 ing and immediate (or future) reactions. In 3-D, twisting flow and eddy-like
207 whirls can significantly add to enhanced mixing by fluid deformation [5, 25].
208 Fluid deformation enhances mixing, which cannot be undone [103, 26]. This
209 mixing is poorly constrained in many grid-based models, leading to incorrect
210 effective reaction rates. The PT reaction theory has been used to estimate the
211 increased reaction rates that may accompany any sort of fluid deformation
212 [43]. This work parallels similar work that examines Eulerian deformation
213 metrics [35, 64] and the similarities may provide a connection between the
214 Eulerian and Lagrangian methods for simulating deformation-enhanced re-
215 actions. In other words, the PT methods provide a computationally simple
216 way to inform larger upscaled grids about the increased reaction rates that

217 are engendered by subgrid fluid deformations.

218 However, it remains to be shown the conditions under which the PT and
219 Eulerian methods converge to the same solutions for a given boundary value
220 problem (BVP). Because mixing-driven reactions can be highly non-linear,
221 the simulated mass of the products and reactants may be highly sensitive
222 to any transport errors. In this work we construct a few simple problems
223 that isolate (and/or eliminate) potential sources of error to investigate the
224 supposed similarity of the methods used to simulate a basic set of n coupled
225 advection-diffusion-reaction equations (ADRE)

$$\frac{\partial C_i}{\partial t} = -\nabla \cdot (\mathbf{v}C_i - \mathbf{D}\nabla C_i) + R(C_1, C_2, \dots, C_n); \quad i = 1, \dots, n, \quad (1)$$

226 where C_i is the concentration of species i , \mathbf{v} is the local mean velocity vector,
227 \mathbf{D} is a dispersion tensor, and $R()$ is a reaction function of all n species.
228 We investigate simulation of dispersion using either a constant $D_{ij} = D_m\delta_{ij}$
229 or a velocity-dependent $D_{ij} = (|\mathbf{v}|\alpha_T + D_m)\delta_{ij} + (\alpha_L - \alpha_T)v_iv_j/|\mathbf{v}|$, where
230 D_m is a diffusion-like constant, $\alpha_L \geq \alpha_T$ are longitudinal and transverse
231 dispersivities, and δ_{ij} is the Kronecker delta. The reaction rate is typically
232 dictated by the law of mass action, and non-equilibrium rates must often be
233 estimated empirically [1].

234 In general terms, any grid-based approximation of (1) will incur several
235 types of error. Foremost is the difficulty in representing a sharp interface
236 with points spaced some distance away from each other in the hyperbolic
237 (advection) portion, along with lesser amounts in the parabolic (dispersive)
238 portion. Additional error in the reaction term arises by representing the var-
239 ious (subgrid) concentration values for each species in a cell by single values.
240 Less obvious are errors incurred in the approximation of the velocity vectors
241 [10], and error from sequentially solving several components of the equation
242 by operator splitting [98]. In any realistic heterogeneous flow field simula-
243 tion, the various errors will have different magnitudes in different regions of
244 the flow domain because of different velocity magnitudes, orientations rela-
245 tive to a grid, and different concentration, velocity, and dispersion coefficient
246 gradient magnitudes and orientations.

247 On the other hand, the discrete and potentially stochastic nature of the
248 PT simulations means that simulation of a deterministic BVP can be nu-
249 merically taxing, as an ensemble of simulations is often needed to ascertain
250 statistics of the solutions. Moreover, the reactions have been shown to depend
251 on the number of particles used: we specify only the positions of particles,

252 so that the initial concentration is approximated by a sum of Dirac delta
253 functions. The initial concentration can only be everywhere equal when the
254 number of particles goes to infinity. Conversely, smaller numbers of parti-
255 cles represent greater heterogeneity in the initial concentration field (in this
256 case, greater correlation length of concentration fluctuations [77]). This het-
257 erogeneity may increase over the duration of the simulation. Finally, it is
258 currently necessary to solve the transport and reactions sequentially, so that
259 error is incurred in the operator splitting. Therefore, it is unclear if the PT
260 simulations will converge to a “correct” solution for a realistic problem, or if
261 a small number of realizations is sufficiently representative of the ensemble
262 mean.

263 Our goal is to compare various aspects of Eulerian and PT simulations
264 of (1). To do so we set up a series of simulations with increasing complexity.
265 The first problem considered here is simple 1- d flow aligned along an x -axis in
266 a 2- d domain. Diffusion is spatially uniform and isotropic. Reaction is limited
267 to a simple (albeit non-linear) irreversible bimolecular system $A + B \rightarrow P$, as
268 this system has been widely used to analyze reactive transport behavior and
269 has been shown to be a fundamental building block of more complex reaction
270 chains [45, 46]. The reaction term in Eq. (1) is $R(C_A, C_B) = -k_f C_A C_B$. For
271 ease of visualization, the product P is made immobile. In uniform flow,
272 all of the advection algorithms used here can be made free of error, so we
273 can isolate diffusion/reaction errors. Following this comparison of PT and
274 Eulerian convergence, a more complex heterogeneous velocity field is used to
275 check the magnitude of errors introduced by Eulerian approximations of the
276 heterogeneous advective fluxes.

277 2. Overview of Error in Eulerian Solutions

278 A common approach to solving the ADRE (1) on a grid is to use oper-
279 ator splitting and sequentially solve the advection, diffusion, and reaction
280 terms. The many algorithms [e.g., 92, 65, 67, 15] for the hyperbolic advection
281 portion are well-known to produce varying degrees of numerical dispersion
282 and/or oscillation and overshoot due to the truncation of higher-order space
283 and time derivatives in the representation of the variability of the concen-
284 tration. We investigate the family of TVD models (including the simplest
285 and best known first-difference upwind weighted scheme) with a forward Eu-
286 ler time approximation on uniform space-time grids of $(\Delta x, \Delta t)$. We choose
287 these algorithms because for a Courant number defined in any direction i by

288 $\lambda = v_i \Delta t / \Delta x_i$ of unity, the advection term is known to be free of numerical
289 dispersion. The Courant number is a measure of how far solute is allowed
290 to traverse any grid block, and most grid-based solutions require $\lambda \leq 1$. In
291 a heterogeneous flow domain, the Courant number is never uniformly unity,
292 and higher-order algorithms that use Courant-based flux limiters are more
293 accurate; however, numerical error is never eliminated entirely from the so-
294 lution, and these algorithms require more computation time. The benefit is
295 a reduction in the number of nodes required to get “equivalent” solutions
296 to the lower-order algorithms. As well, many other schemes can be adopted
297 to manage the error and computational cost of Eulerian methods including
298 adaptive refinement of grids where necessary (e.g., [50]) or more accurate
299 timestep interpolation (e.g., [93]). However, there is no consensus on the
300 most appropriate algorithm, and solutions based on 1st-, 2nd-, and 3rd-order
301 accuracy in space on uniform grids are common.

302 Generally speaking, the discretized diffusion operator is thought to be
303 sufficiently error-free, relative to any advective error. On the other hand,
304 application of the law of mass action for the reaction term assumes perfect
305 mixing within any Eulerian block. The effect of subgrid concentration per-
306 turbations are not resolved by the numerical method. Recent studies have
307 focused on this effect and shown that incomplete mixing effects can be strong,
308 leading to significantly altered reaction rates [11, 77, 76, 23, 80] compared to
309 those predicted by the assumption of perfect mixing. The non-linear nature
310 of the reactions can make the simple act of concentration averaging highly
311 variable [e.g., 7, 8, 88]. Newer formulations of the reaction term can account
312 for subgrid concentration variability by assuming both a distribution of con-
313 centration and a subgrid mixing rate, but this method requires calibration
314 with measured reactions at the appropriate scale (e.g., [23]). In short, the
315 “spikier” the unknown subgrid concentration heterogeneity and the more
316 nonlinear the reaction, the greater the averaging error that will occur.

317 **3. Overview of Error in Lagrangian Solutions**

318 In the PT simulations at hand, the advection of individual particles can
319 be made essentially free from error by using Pollock’s algorithm [79]. For the
320 explicit Euler approximation we use here, the advection error is negligible as
321 long as the velocity field is fairly smooth [10]. The diffusion operator can be
322 made arbitrarily accurate in the mean by using motions that solve the correct
323 Fokker-Planck equation [60, 9, 85]. For example, if a spatially heterogeneous

324 dispersion equation is being solved, then the motions are generated according
325 to an Itô implementation of the nonlinear Langevin equation for Gaussian
326 random walks ([60, 85], and see Appendix C). If post-simulation reconstruc-
327 tion of the concentration field is required, errors arise with variance related to
328 the particle numbers, binning size and smoothing kernels used [e.g., 22, 78].
329 A similar problem to the “subgrid” concentration fluctuation is present for
330 PT methods, in that a sufficient number of particles must be used to resolve
331 the small-scale correlation structure of the concentration fields [39].

332 There are several methods for calculating the chemical reactions among
333 the particles. Many are based on an on-off (binary) type of reaction cal-
334 culation based on the hard-shell particle “radius” model [102, 41]. If two
335 particles are located within this radius, then a reaction takes place [42, 49].
336 Others are based on a calculation of the probability that two particles will
337 be collocated based on dispersion motion [101, 11]. This method is readily
338 extended to spatially nonlocal dispersion [e.g., 16]. The co-location proba-
339 bility is then multiplied by the conditional probability that two co-located
340 particles will react. This latter probability is a simple statement of the ther-
341 modynamic reaction rate [46, 54] so the particles are not forced to react (i.e.,
342 slow reactions may require multiple co-locations, while fast ones may require
343 very few before a reaction actually occurs). In these models, no lattice is
344 used, so the separations are real-valued and the probability of collision is not
345 binary. This approach can be made arbitrarily accurate without the need for
346 empirical parameters [77]. Bolster et al. [18] extend the algorithm by replac-
347 ing the probability of conversion with a particle mass-fraction loss. Their
348 algorithm gains resolution of low concentrations but has not been rigorously
349 tested for convergence to the original particle birth-death algorithm, so we
350 partially address this issue here. In particular, the original bimolecular al-
351 gorithm of *Benson and Meerschaert* [11] converts entire reactant A and B
352 particles into entire product P particles, so that number of $A + P$ particles
353 remains constant in these simulations. However, the lowest possible resolved
354 concentrations are $\mathcal{O}(1/N_A)$, where N_A is the original number of A particles.
355 *Bolster et al.* [18] convert portions of each particle’s mass during a reaction,
356 so that low concentrations are infinitely resolvable, but: 1) numerically, a
357 nearby P particle must be located, or 2) the product mass must be mapped
358 to a fixed grid of concentration, given some binning procedure. Here we
359 choose the latter with product mass mapped to the nearest square grid.

360 4. Convergence of the Diffusion/Reaction Operations

361 Because we later investigate the solutions in heterogeneous 2- d velocity
362 fields, we first choose identical 2- d solutions with homogeneous velocity to
363 isolate the diffusion/reaction portion of the ADRE. A series of simulations
364 was constructed using geologically-relevant parameters for transport and in-
365 teraction of two fluids in a 1000 m \times 1000 m aquifer domain. Two fluids
366 are placed next to each other in 15.6 m strips, separated by an initially
367 sharp interface (Fig. 1a). The aquifer has a mean hydraulic conductivity
368 $K = 1$ m/d, a uniform head gradient in the x -direction of 0.01, and a poros-
369 ity of 0.3. The fluid velocity is uniform at 1/30 m/d aligned with the x -axis.
370 The dispersion is made uniform and isotropic at 0.001 m²/d, representing
371 an isotropic local dispersivity of 0.03 m. It is made homogeneous to allow
372 comparisons with 1- d analytic models (Appendix B). The fluids are placed at
373 mean concentrations of 1 M (molar), and the reaction follows the law of mass
374 action $R(C_A, C_B) = -k_f C_A C_B$ with rate coefficient $k_f = 0.01$ (M d)⁻¹. We
375 assume unit activity coefficients for simplicity. This rate was chosen so that
376 a significant fraction of the reactants (on the order of 20%) will be consumed
377 after 10,000 days of transport in the simplest case. Approximate measures
378 of the reaction versus transport rates are given by either the advective or
379 diffusive Damköhler numbers $Da_v = k_f C_0 / (\mathbf{v}/L)$ and $Da_D = k_f C_0 / (D/L^2)$,
380 where L is a characteristic scale of transport. For local-scale Da , we choose
381 $L \approx 1$ m, so for the uniform velocity case, we have $Da_v \approx 0.3$ and $Da_D \approx 10$.
382 Neither of these numbers point to particularly slow or fast reactions relative
383 to transport.

384 To compare the grid-based and PT codes, we should choose similar initial
385 conditions (ICs). It has been shown that the PT codes inherently represent
386 spatial variability in the initial condition and also as the particles diffuse and
387 react: the spatial autocovariance decreases with increased particle number.
388 *Paster et al.* [77] show that, for the Dirac-delta function particles that we
389 use here, the initial particle number N_0 is related to the auto-covariance
390 structure of the initial concentrations by $N_0 = C_0^2 A_{strip} / (\sigma_C^2 l^d)$, where A_{strip}
391 is the area over which the particles are placed, and $\sigma_C^2 l^d$ is the d -dimensional
392 integral of the covariance function (i.e., the concentration variance times the
393 d -dimensional correlation length). The concentration IC becomes smoother
394 as the number of particles gets larger. Therefore, for the grid-based codes
395 we choose initial concentrations that are deterministically uniform. We also
396 uniformly and randomly distribute the particles in the same size strips as in

397 the Eulerian codes (Fig. 1) and vary the number of particles.

398 4.1. L^1 convergence

399 The Eulerian code was run at different discretizations while holding the
400 Courant number $\lambda = 1$. The first check of convergence is the integrated mass
401 of product after 10,000 days (i.e., the spatial L^1 convergence). The Eulerian
402 solutions appear to converge in this sense at $\Delta x \leq 1$ m and a total reaction
403 completion of 22.08% (Fig. 2). Because of the 2- d nature of the problem
404 and a low-to-intermediate value of $Da_v \approx 0.3$, we only have an approximate
405 analytic solution to this problem (Appendix B.1), so the check of convergence
406 is relative stability of the solution at 22.08%.

407 Because the initial particle locations and the dispersion motions both have
408 random components, the PT simulations are stochastic in nature: each solu-
409 tion will give slightly different results. Here we show the mean and standard
410 deviations of the integrated mass of product for an ensemble of 20 particle-
411 killing simulations (Fig. 2). The non-deterministic nature implies that the
412 initial conditions have some inherent randomness that should be constructed
413 to represent the actual physical heterogeneity [39]. The number of particles
414 encodes the spatial autocorrelation of initial concentrations, and simulations
415 with different number of initial particles are supposed to give different re-
416 sults. Therefore, our check of convergence follows two tacks: varying the
417 number of particles and the time-step size. As the former becomes larger,
418 the effective concentration correlation length becomes a smaller fraction of
419 the size of the specified initial condition structure (i.e., a better-mixed I.C.)
420 and should mimic the homogeneous deterministic initial condition and so-
421 lution given by the Eulerian simulations. Indeed, increasing the number of
422 particles shows this kind of convergence to a reaction completion of 22.10% in
423 the particle-killing simulations (Fig. 2). The inter-simulation variability also
424 decreases when the particle density increases, as expected. It appears that
425 the converged Eulerian (with $\Delta x = 0.98$ m) and Lagrangian solutions are
426 very similar when the initial number of A and B particles is 20,000 (22.05%
427 and 21.94% respectively).

428 We also checked the solutions when the timestep size was varied, and
429 also checked the newer algorithm [18] that does not kill reactant particles
430 (instead, the particle masses are allowed to decrease). These simulations are
431 more accurate at lower concentrations with the tradeoff of longer simulation
432 times. We checked the simulations for initial particle numbers of 10,000
433 at different Δt over a very large range. The means of the particle-killing

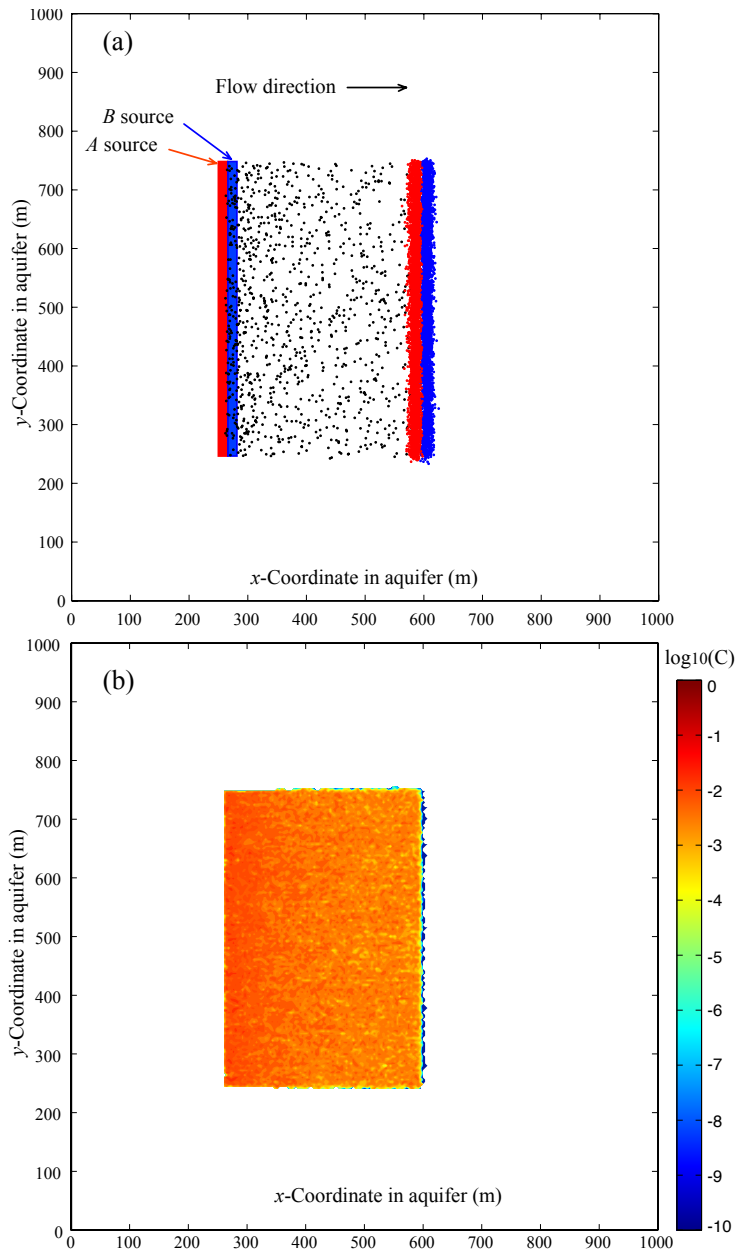


Figure 1: a) Aquifer domain showing location of initial reactants A (red rectangle) and B (blue rectangle) for both PT and Eulerian simulations. Also shown are the single-realization locations of individual particles of product P (black) and reactants A (red) and B (blue) for initial particle numbers $N_A(t=0) = N_B(t=0) = 5,000$. b) Base-10 logarithm of binned product concentrations (colorbar shows $\log_{10}(\text{Molar})$) from an ensemble of 10 particle-number preserving [18] simulations, using bin size of $\Delta x = \Delta y = 4$ m. The colorbar is scaled to match later plots - it does not show all of the low-concentration detail.

434 and particle-preserving algorithms are not statistically significantly different
 435 at the particle number and timestep resolutions duplicated here (Figure 2
 436 inset).

437 As explained by Paster et al. [77] (and reiterated by Hansen et al. [49]),
 438 there is a potential for multiple particle collisions during a single timestep
 439 that may be under-estimated by large Δt . The neglect of the diminishing
 440 survival probability should tend to over-estimate reactions for too large a
 441 Δt . On the other hand, too small a timestep reduces the area “probed”
 442 by a particle and reduces the number of potential reaction partners, until,
 443 as $\Delta t \rightarrow 0$, only the nearest neighbors are allowed to react. So too small
 444 a timestep should tend to underestimate reaction rates. The correct Δt
 445 lies between a lower value dictated by the average particle density and an
 446 upper number dictated by several stability criteria. We may bracket the
 447 timestep size by the ratio of the effective search radius for a particle pair
 448 undergoing diffusion to average particle spacing $0.25 < 2\sqrt{8D_m\Delta t}/\Delta x <$
 449 1.5 [77]. The factor 8 in the square root differs from pure diffusion and
 450 comes from the convolution of two Gaussians representing the co-location
 451 probability (Appendix C). The initial condition area A_{strip} over the particle
 452 number of one species $N_A(t)$ gives a first-order approximation of inter-particle
 453 spacing. In the simulations at hand, $D_m = 0.001m^2/d$, and average inter-
 454 particle distance $A_{strip}/N_A(t=0) \approx 0.78m$, so $1.2d < \Delta t < 340d$. Varying
 455 the timestep over a wide range shows that the solutions have an inflection
 456 point between too little and too much reaction at the point surrounding the
 457 smaller of the two values (Fig. 2 inset). From approximately $\Delta t \leq 10$, the
 458 mean product concentrations are not significantly different, so in general we
 459 recommend setting $\Delta t < 0.16\Delta x^2/D_m$.

460 4.2. Pointwise (L^∞) convergence

461 Because the Eulerian simulations are deterministic, we may also look
 462 at the shapes of the product distributions to assess qualitatively the point-
 463 wise convergence (Fig. 3). The peak concentrations in the 1st-order upwind
 464 simulations continue to rise significantly over the range of discretizations
 465 tested (the finest discretization model comprised over 4 million cells), so
 466 that pointwise convergence was not seen in these simulations. Similar, but
 467 lower magnitude, issues were seen in simulations using 2nd- and 3rd-order
 468 TVD simulations (Appendix A). If maximum concentrations are a concern
 469 to the user, a finer discretization will be required than one derived (later in
 470 this paper) for accuracy in the L^1 norm.

471 In the PT simulations, the concentrations are only created by binning
 472 the particles, hence the concentrations will be functions of bin size and any
 473 kernels used to model the spatial influence of particles (see, e.g., Fig. 1b). In
 474 an effort to compare to the Eulerian results, the mean concentrations along
 475 the centerline of the product plume for ensembles of simulations are compared
 476 (Fig. 4). The concentrations are simple sums of particle masses in square
 477 cells of size $\Delta x = 4$ m. A similar effect in the PT relative to the Eulerian
 478 simulations is found when the number of initial particles increases: more
 479 particles tend to resolve higher peak mean concentrations. The effect is not
 480 enhanced a great deal by the choice of bin size; however, bigger bins will tend
 481 to smooth out the higher peak concentrations (Fig. 4). Furthermore, those
 482 PT simulations that have total masses of product similar to the Eulerian
 483 simulations (for example, 20,000 particles corresponding to $\Delta x = 0.98$ m)
 484 also have similar mean peak concentrations. It should be noted that there
 485 is considerable variability in the binned product concentrations from the
 486 particle-killing algorithm along the plume direction. For example, at the peak
 487 location in the 50,000 particle, 256 bin simulation, the product concentrations
 488 had a standard deviation of approximately 0.0065 M (compared to the mean
 489 concentration of 0.037 M).

490 5. Eulerian Velocity Error

491 The spatial approximation using 1st-order upwind advection scheme used
 492 here has a known numerical dispersion of magnitude $\frac{|v|\Delta x}{2}(1-\lambda)$ [66]. A simi-
 493 lar magnitude error is incurred by the forward Euler time-stepping, so the the
 494 total error is of order $|v|\Delta x(1-\lambda)$. Here we investigate 1) the combined effect
 495 of changing both Δx and λ in a simple homogeneous velocity field and 2) the
 496 effect of spatially variable λ in a more realistic heterogeneous field. We also
 497 implement a 3rd-order TVD and the particle-number-preserving Lagrangian
 498 algorithms on the same velocity fields.

499 5.1. Homogeneous Velocity

500 For the homogeneous velocity case, the Courant number λ was varied
 501 between 0.1 and unity for three levels of discretization ($\Delta x = 0.49, 0.98,$
 502 and 1.95). The reacted masses at 10,000 days increased, in some cases
 503 dramatically, at all $\lambda < 1$ (Fig. 5) due to spurious numerical dispersion
 504 and erroneous mixing, particularly in the 1st-order upwind algorithm. The
 505 amount of product doubled or tripled at the lowest Courant numbers and

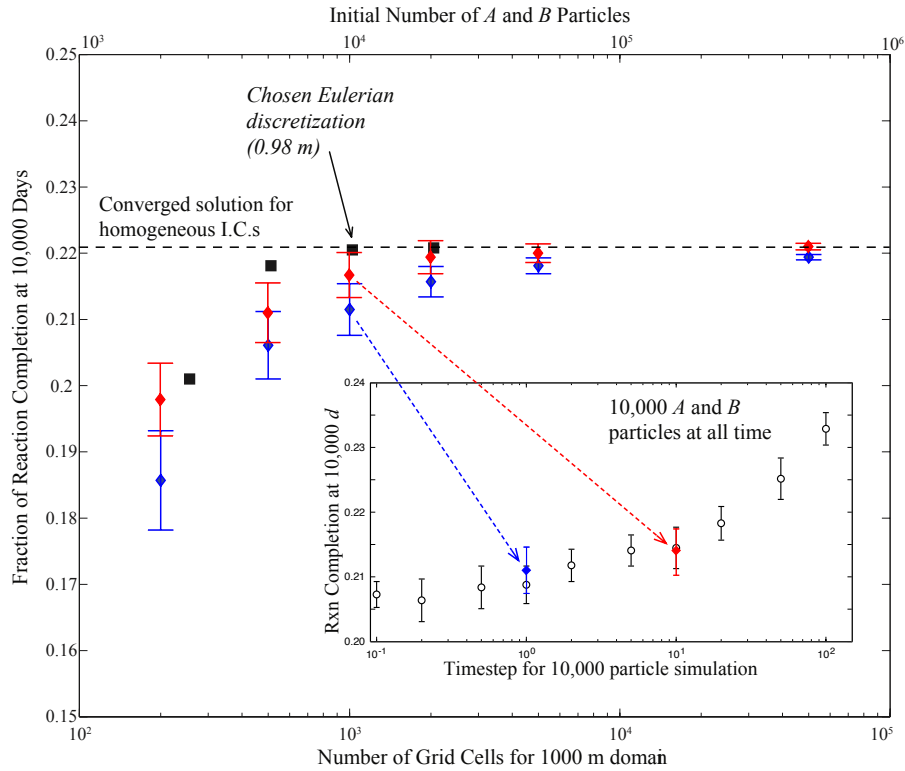


Figure 2: Degree of reaction completion within Eulerian (solid squares) and PT simulations (whiskers denoting $\pm 1\sigma$). Red and blue denote $\Delta t = 10$ and 1 d, respectively. The top x-axis represents initial number of both A and B particles; the bottom x-axis is the number of finite-difference grids for 1,000 m domain (i.e., $\Delta x = 1,000/N_g$ m). All solutions appear to converge to a reaction completion of 22.1%. Based on similarity, convergence, and speed of solution, the “base-cases” of 40,000 particles and 1024 finite-difference grids (both highlighted) are chosen.

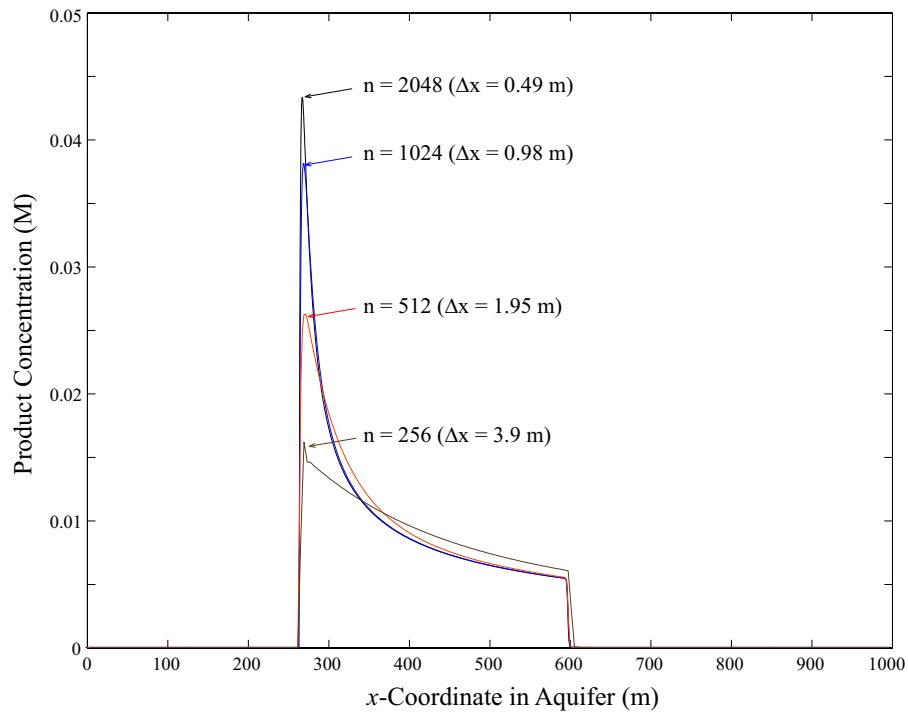


Figure 3: Product concentrations along horizontal slices of the aquifer for all upstream Eulerian schemes (because all have zero numerical dispersion for Courant number $\lambda = 1$) using different discretizations. Any deviations are due to different mixing at different discretizations.

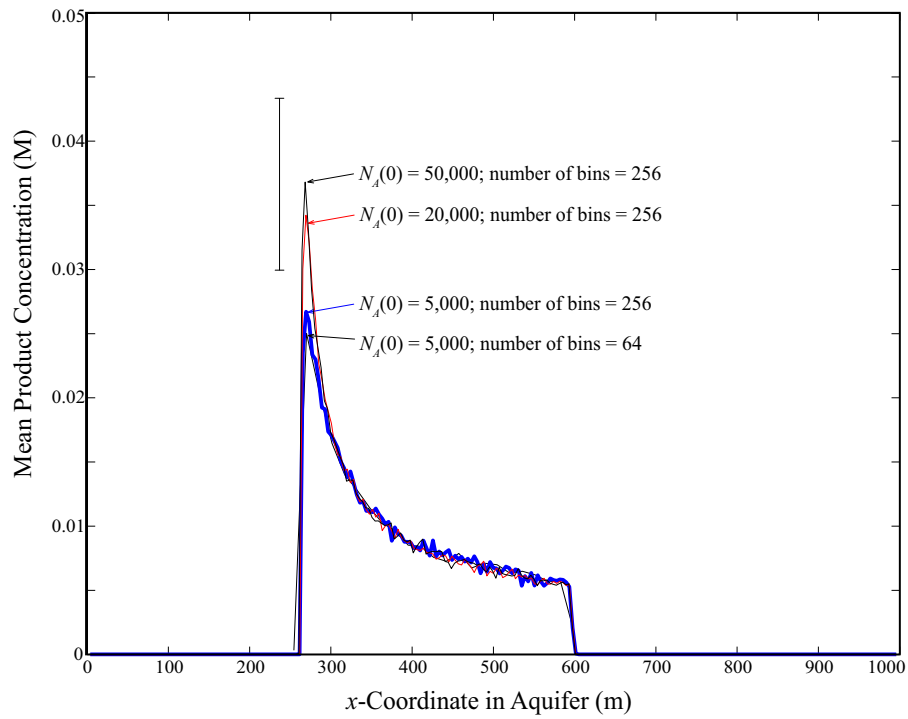


Figure 4: Averaged product concentrations from particle-killing PT simulations along horizontal slices of the aquifer using different number of initial particles $N_A(0)$ and bin sizes (indicated by number of bins in x -direction). The vertical whisker bar denotes $\pm 1\sigma$ for the 50,000 particle peak concentration.

506 highest Peclet numbers. In Appendix B we demonstrate semi-analytically
 507 how changes in dispersion coefficient might affect the total mass of product
 508 produced. The total mass of product produced, for either fast or slow bi-
 509 molecular reactions, scales approximately as \sqrt{D} , meaning that any errors in
 510 D , arising from numerical dispersion, can result in significantly larger masses
 511 of product. For 1st-order, explicit forward Euler solutions, the numerical dis-
 512 persion has a maximum on the order $|v|\Delta x$ so the the grid Peclet number
 513 ($P_g = v_{max}\Delta x/D$) is a measure of the ratio of spurious to real dispersion.
 514 For velocity-dependent dispersion this reduces to $P_g \approx \Delta x/\alpha_L$. A value of
 515 $P_g = 2$ means that real and spurious dispersion are of the same order, and
 516 excess product on the order of $\sqrt{2}$ times the correct amount is produced.
 517 In general, the maximum amount of error is approximately $\sqrt{1 + P_g/2} - 1$,
 518 so that obtaining 5% mass error from a 1st-order accurate algorithm would
 519 require $P_g \approx 0.2$.

520 The 3rd-order TVD scheme appears to give reasonable reaction totals (in
 521 the integrated L^1 sense) over a large range of λ for $\Delta x \leq 0.5m$, which
 522 corresponds to a classical $\Delta x/\alpha_L \leq 16$. Note that for the particle tracking
 523 schemes the results with advection are identical to those without advection
 524 presented in the previous section due to the principle of Galilean invariance
 525 (i.e., a uniform advection merely shifts all particle locations, but does not
 526 change their relative distance from one another, which is all that is required
 527 for reaction).

528 The peak concentrations in these Eulerian simulations were also tracked,
 529 and at all discretizations there were substantial errors introduced by the
 530 advection approximations (Fig. 6). Although not shown here, the 3rd-order
 531 advection algorithm converged to less than 5% error in this L^∞ sense at about
 532 $\Delta x = 0.1m$, while at this smallest discretization (representing $P_g = 4$) the 1st-
 533 order had peak concentrations approximately 50% too high. Also noticeable
 534 in these plots is the error due to the diffusion and reaction operators at a
 535 Courant number of unity. These numbers correspond to the different peak
 536 concentrations shown in Fig. 3.

537 5.2. Spatially Variable Velocity

538 A random fractal K field with anisotropic-, or operator-scaling, was gener-
 539 ated using Fourier filter methods [13]. Operator-scaling in this context
 540 means that transects of the K field are fractional Brownian motions with
 541 different Hurst coefficients in the x - and y -directions of 0.44 and 0.36 (with
 542 uniform weighting on the axes) so that there is greater correlation of the

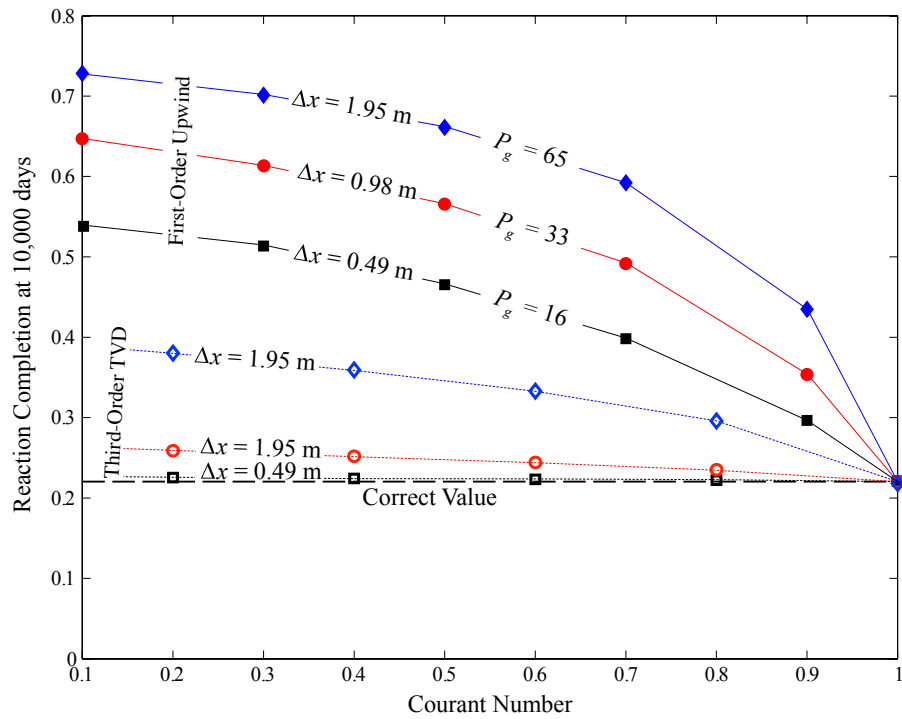


Figure 5: Amount of product produced in Eulerian simulations at 10,000 days by the 1st-order upwind (filled symbols) and 3rd-order TVD schemes (open symbols) with different space and time discretizations. Lines added to aid visualization.

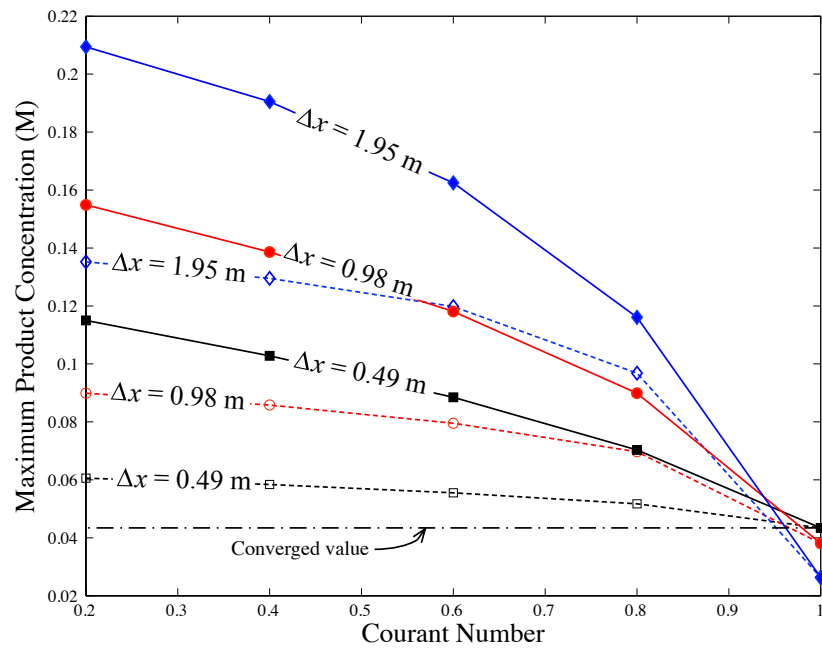


Figure 6: Maximum product concentration in Eulerian simulations at 10,000 days by the 1st-order upwind (filled symbols, solid connecting lines) and 3rd-order TVD schemes (open symbols, dashed connecting lines) with different space and time discretizations. Lines added to aid visualization.

543 underlying Gaussian increments in the x -direction (Fig. 7). The geomet-
544 ric mean K is 1 m/d to match the uniform velocity field in the previous
545 section. The porosity is set to 0.3 and the mean hydraulic gradient to 0.01.
546 The K and steady-state velocity fields were calculated using a block-centered
547 scheme at a uniform discretization of $\Delta x = \Delta y = 0.98$ m. To illustrate the
548 general features of the velocity field, a line of uniformly-spaced inert par-
549 ticles was placed along a transect at the initial A/B reactant interface at
550 $x = 256$ m (Fig. 8) and tracked at 1000-day intervals (with a blue line
551 joining initially adjacent particles). The lines and particles allow a rough
552 estimation of the local components of fluid deformation, including shear and
553 dilation/compression transverse to the mean flow direction. Because of the
554 divergence-free (incompressible) flow, any dilation in the flow direction must
555 be accompanied by compression in the orthogonal direction and vice-versa
556 [35, 43].

557 *5.2.1. Isotropic, Spatially Constant Dispersion*

558 Fluid deformation, including shear, can put reactants into closer prox-
559 imity and increase reaction rates [43], as verified visually by the locations
560 of generated product particles (mapped to $\log_{10}(\text{concentration})$ on a grid of
561 0.98×0.98 m cells) in a 40,000-particle simulation (Fig. 9d). The regions of
562 high deformation, as indicated by stretching and/or shearing flowlines, are
563 expected to be regions of extremely high or hyper-mixing [17, 35]. Indeed
564 they tend to be heavily populated with product particles (Fig. 9d). The to-
565 tal amount of product, i.e., the completion of the reaction after 10,000 days,
566 is 37.4% in this simulation, or roughly 70% greater than the total amount of
567 product (22.1%) in the homogeneous domain, all other factors being equal.
568 This increase is due entirely to fluid deformation. An ensemble mean of 10
569 simulations shows the same features (Fig. 9c), demonstrating that the strong
570 zonation of reaction intensity is not an artifact of random variations between
571 realizations.

572 The Eulerian solutions have unphysical negative concentrations spread
573 throughout the lower-concentration regions, so only concentrations greater
574 than 10^{-20} are shown here. A 1st-order Eulerian simulation with the same
575 velocity field and parameters with $\Delta x = \Delta y = 0.98$ m (or a domain of
576 $1024 \times 1024 \approx 10^6$ nodes) gives a total amount of product of 53%, or roughly
577 double the increase seen in the PT simulations going from homogeneous to
578 the heterogeneous velocity fields (Fig. 9a). This overestimation is consistent
579 with the overestimations by the Eulerian simulators in a homogeneous do-

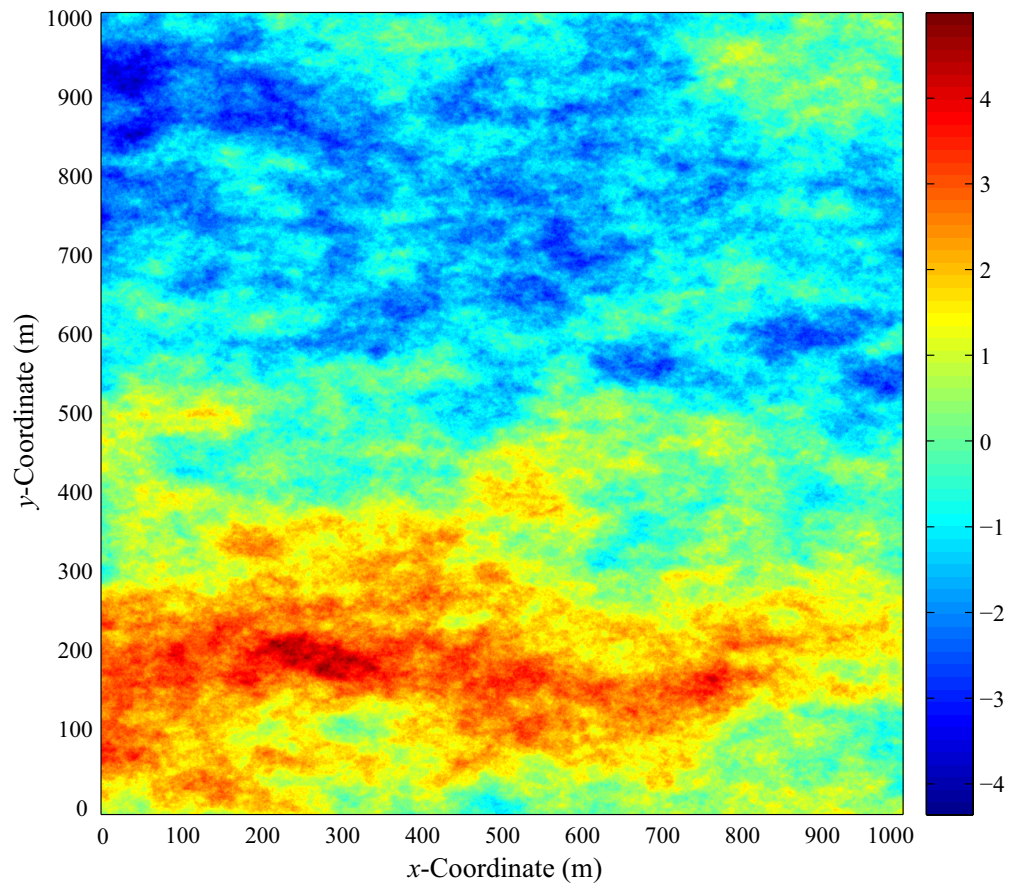


Figure 7: Anisotropic, or matrix-scaling fractional Brownian motion K field. Color bar represents values of $\ln(K)$ in m/d.

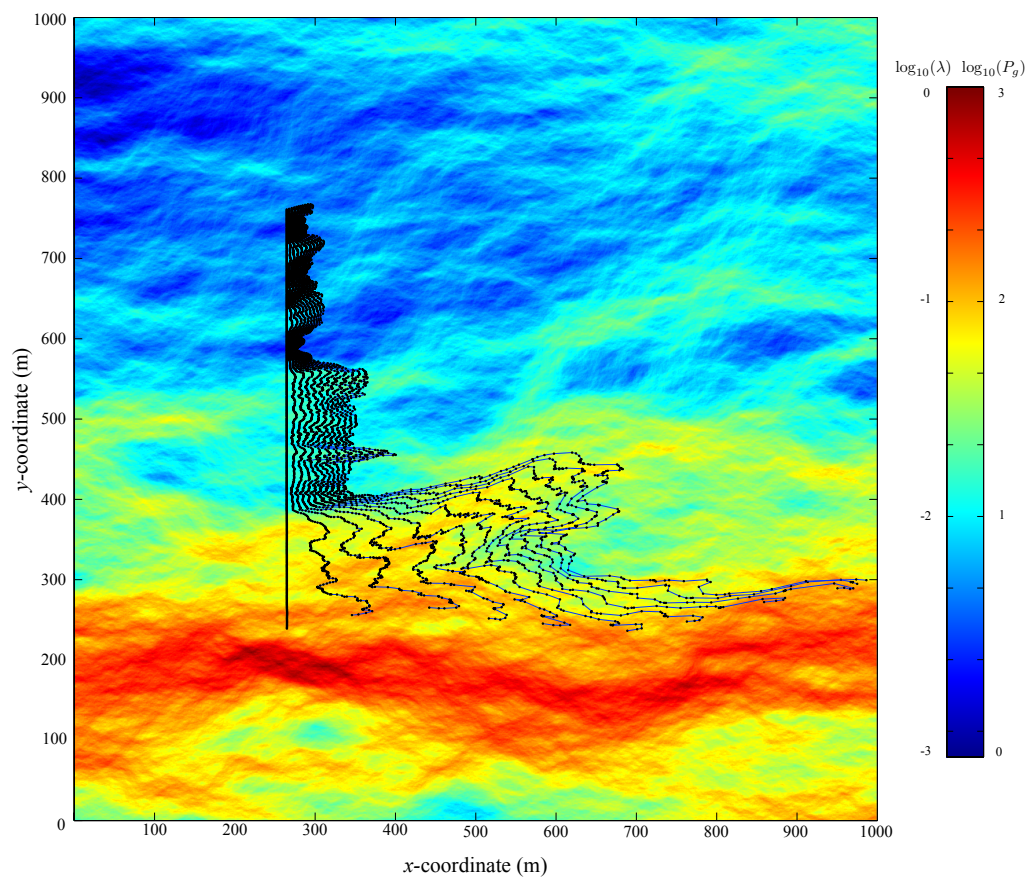


Figure 8: Pure advection of a line of 500 particles (black dots) initially placed at the location of reactant interface $x = 256$ m. The blue line connects initially adjacent particles that were placed 1 m apart. The background colors are the logarithm of velocity magnitudes, with higher velocities represented by warmer colors. The colorbar shows the velocities converted to Courant (λ) and grid Peclet (P_g) numbers. Highlighted areas show regions of shear, compression, and dilation relative to local flow direction.

580 main for smaller Courant numbers (Fig. 5). Calculated velocities in the het-
 581 erogeneous domain spanned over three orders-of-magnitude; therefore, the
 582 local Courant numbers go from essentially zero to unity across the entire
 583 domain (Fig. 8). The numerical dispersion in both the longitudinal and
 584 transverse directions (because flow is seldom exactly parallel to the x -axis
 585 in the heterogeneous flow field) leads to substantial overestimation of the
 586 spatial extent of reaction in both high and low velocity zones (Fig. 9a). The
 587 1st-order Eulerian method does not resolve the fine “threading” of reaction
 588 that takes place in areas of high fluid deformation.

589 The 3rd-order TVD method is visually better at restricting spurious lat-
 590 eral dispersion and preserving structure within the plume (Fig. 9b), and has
 591 an integrated product concentration closer to the PT simulations (at 39.4%).
 592 For this algorithm, another level of grid refinement (at a cost of 8 times the
 593 computation time, addressed in a subsequent section) would be necessary
 594 for the simulation to adequately match the PT results. For the first-order
 595 algorithm, the values of Δx and Δt would need to be reduced to bring the
 596 grid Peclet numbers substantially below unity to reduce numerical mixing to
 597 less than the real mixing (see Appendix B). In the example used here, on
 598 the order of 1 to 100 billion cells would be required, which is far outside the
 599 computational resources available to us.

600 5.2.2. Anisotropic, Velocity-Dependent Dispersion

601 All of the transport and reaction algorithms are straightforward to ex-
 602 tend to velocity-dependent and anisotropic dispersion (??). The dispersion
 603 coefficient (and local dispersivity) at this scale represent subgrid velocities
 604 that are not resolved and are a function of flow field variability. Because
 605 we are not following the assumptions of low velocity variability and finite
 606 and fixed correlation lengths, there are no analytic expressions for effective
 607 block dispersivity [34]. Instead we use a common assumption that sub-grid
 608 dispersion is some fraction of the size of the block (the size at which velocity
 609 is resolved). Here we chose $\alpha_L = 0.1\Delta x$, where Δx was held at 0.98 m based
 610 on the resolution of the velocities. The timestep size was chosen to maintain
 611 $\lambda = 1$ at the highest velocity (which is constant for the Eulerian simulations
 612 but may change based on the highest velocity experienced at any time by
 613 the particles).

614 Due to the lower values of dispersion in low-velocity areas (compared to
 615 the previous example with $\mathbf{D} = 0.001 \frac{m^2}{d} \mathbf{I}$), the particle-number-preserving
 616 PT simulations have lower integrated reaction product of 29.4% relative to

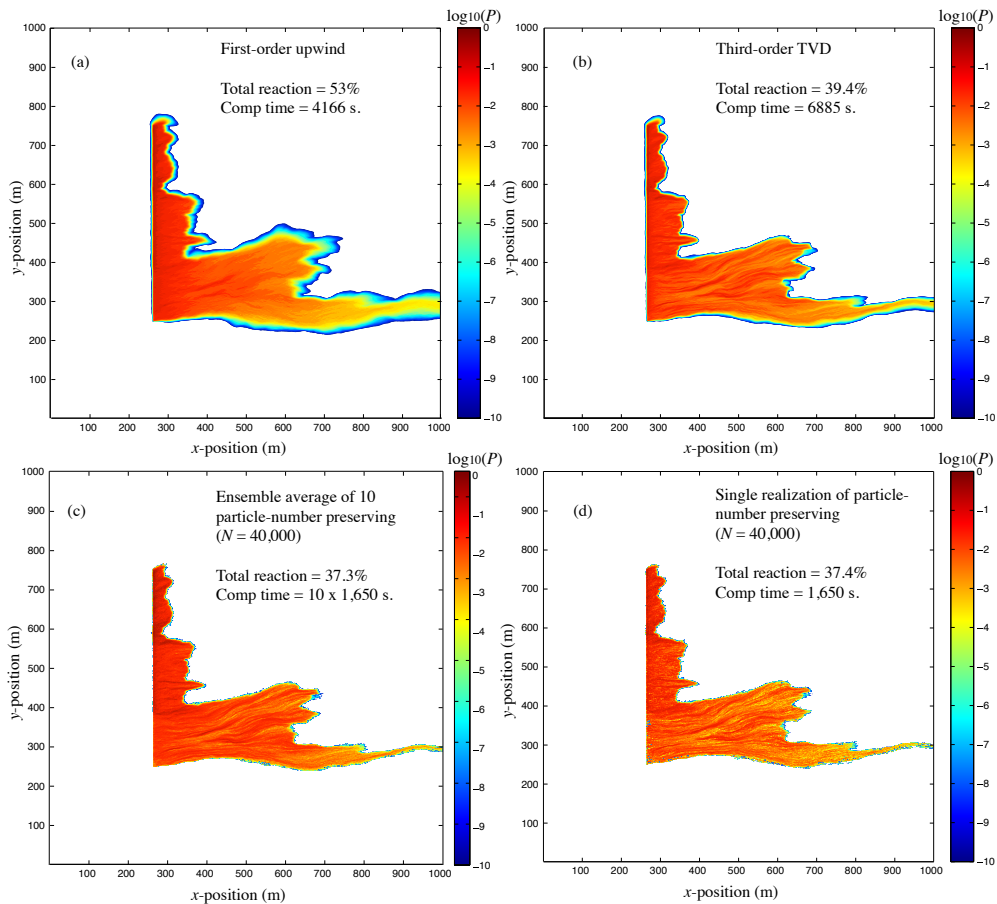


Figure 9: Base-10 logarithms of simulated product concentrations at 10,000 days using constant $D = 0.001m^2/d$: a) (Eulerian) first-order upwind, b) (Eulerian) third-order TVD, c) Ensemble average of particle-preserving PT, and d) Single realization from (c). Colorbars denotes Molar product concentration. Eulerian simulations have large areas of negative concentrations, so plots only show concentrations above 10^{-20} M.

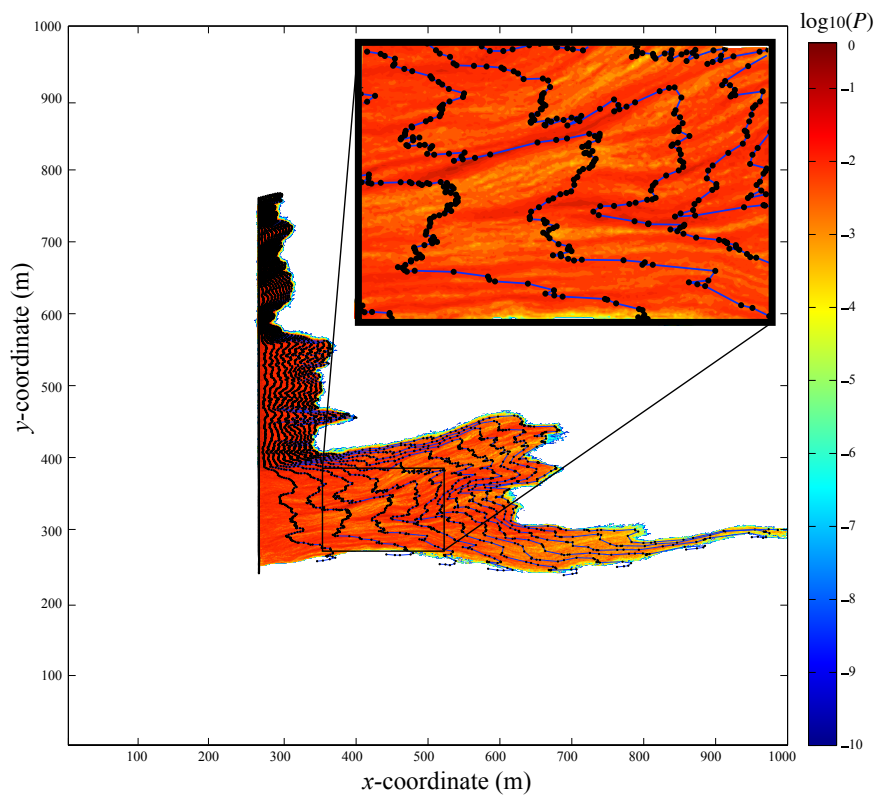


Figure 10: Overlay of advection-only particle traces (Fig. 8) above base-10 logarithms of simulated product concentrations at 10,000 days from an ensemble average of particle-preserving PT (reproduced from Fig. 9d). Higher reaction rates are consistently found in places where the fluid deformation shows folding and compression lateral to mean flow. Colorbar denotes Molar product concentration.

617 the 37.4% in the isotropic **D** case (Figs. 11 c and d).

618 For the 1st-order upwind simulations, the common block-size based dis-
619 persivity choice gives $P_g = 10$. This simulation is very similar, both vi-
620 sually and quantitatively, to the previous isotropic **D** simulation (compare
621 Figs. 9a and 11a). Each 1st-order simulation indicates reaction completion
622 at about 50% — neither can resolve the subtle differences in the formulation
623 of dispersion. The mixing is dominated by error. The 3rd-order simulation
624 over-estimates the reactions by several percent (at 33.8%), consistent with
625 the isotropic dispersion and homogeneous velocity cases. However, for both
626 Eulerian simulations, spurious over-mixing in the source area, combined with
627 excess transverse dispersion, depletes the reactants far downstream so that
628 the peak concentrations modeled at the exit area of the aquifer are roughly
629 3 to 10 times lower than in the PT simulations (compare exit zones in Figs.
630 11a-d).

631 A clear feature of the more accurate PT and 3rd-order simulations is the
632 high degree of variability and structure of the product distribution in space
633 (Figs. 11b-d). There is more structure in this simulation than the isotropic
634 **D** case because of the lower values of transverse dispersion, which limits mix-
635 ing where the reactant interface has been sheared or folded. A comparison of
636 cross-sections of the product concentrations in the middle of the plume (Figs.
637 12 a-b) shows that the ensemble mean PT and 3rd-order simulations are in
638 agreement, but that a single realization, which represents a potential path-
639 way of an initially heterogeneous plume, has substantially greater variability.
640 Even at a mean transport distance of ≈ 250 , some product concentrations
641 are 100 times different within ≈ 5 meters of each other. The peaks and
642 valleys are co-located in the single realization and ensemble plumes, but the
643 combination of fluid deformation and perturbed concentrations in the initial
644 conditions are amplified by the nonlinear reaction. The first-order Eulerian
645 simulation is a poor indicator of reaction heterogeneity.

646 5.3. Computation time

647 For a consistent means of comparing computation times, all of the codes
648 were implemented in Matlab on a laptop machine with a 2.7 GHz Intel Core
649 i7 processor and 8GB of 1333 MHz DDR3 RAM (and OSX 10.9.5 operat-
650 ing system). As long as there is enough RAM space, a table of execution
651 times (Fig. 13) verifies that the Eulerian codes require a minimum time
652 $T \approx K_1 \Delta x^{d+1} + K_2$, where T is execution time [s], d is the number of di-
653 mensions ($d = 2$ here), K_1 is a constant that depends on the number of

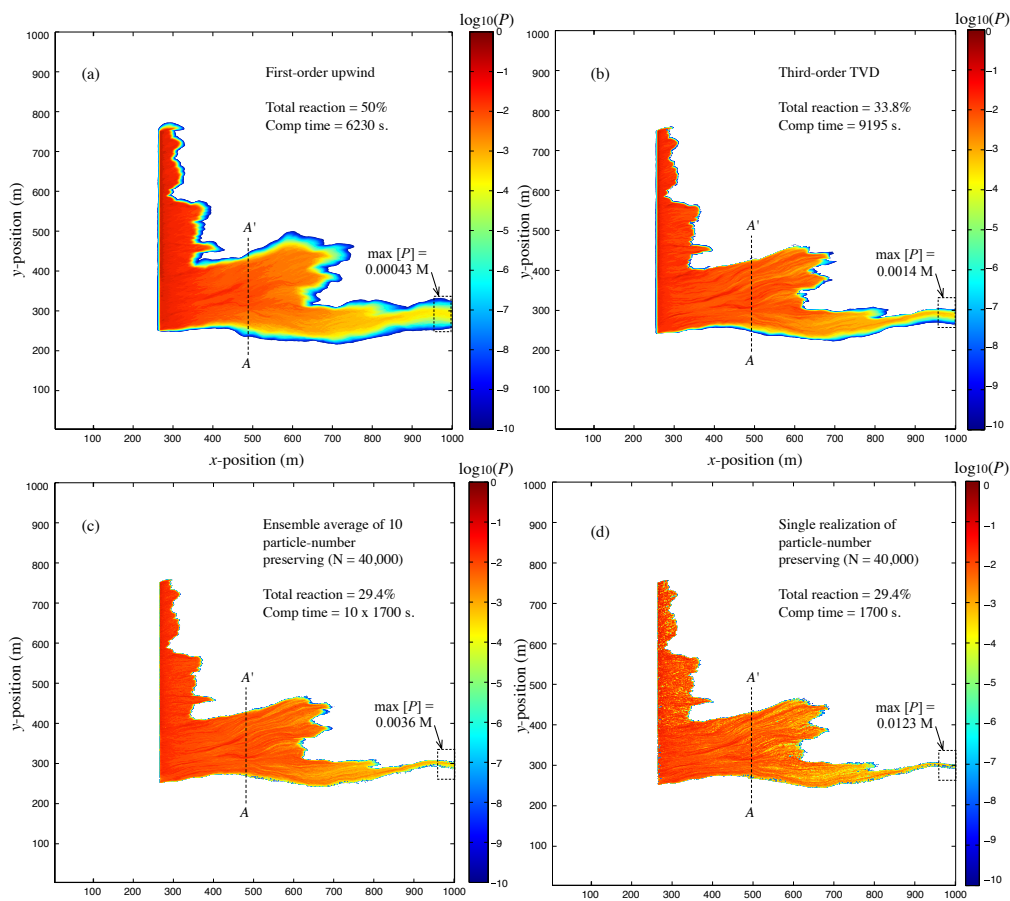


Figure 11: Base-10 logarithms of simulated product concentrations at 10,000 days using velocity-dependent D with $\alpha_L = 0.1m$: a) (Eulerian) first-order upwind, b) (Eulerian) third-order TVD, c) Ensemble average of particle-preserving PT, and d) Single realization from (c). Colorbars denotes Molar product concentration. Eulerian simulations have negative concentrations, so plots only show concentrations above 10^{-20} M.

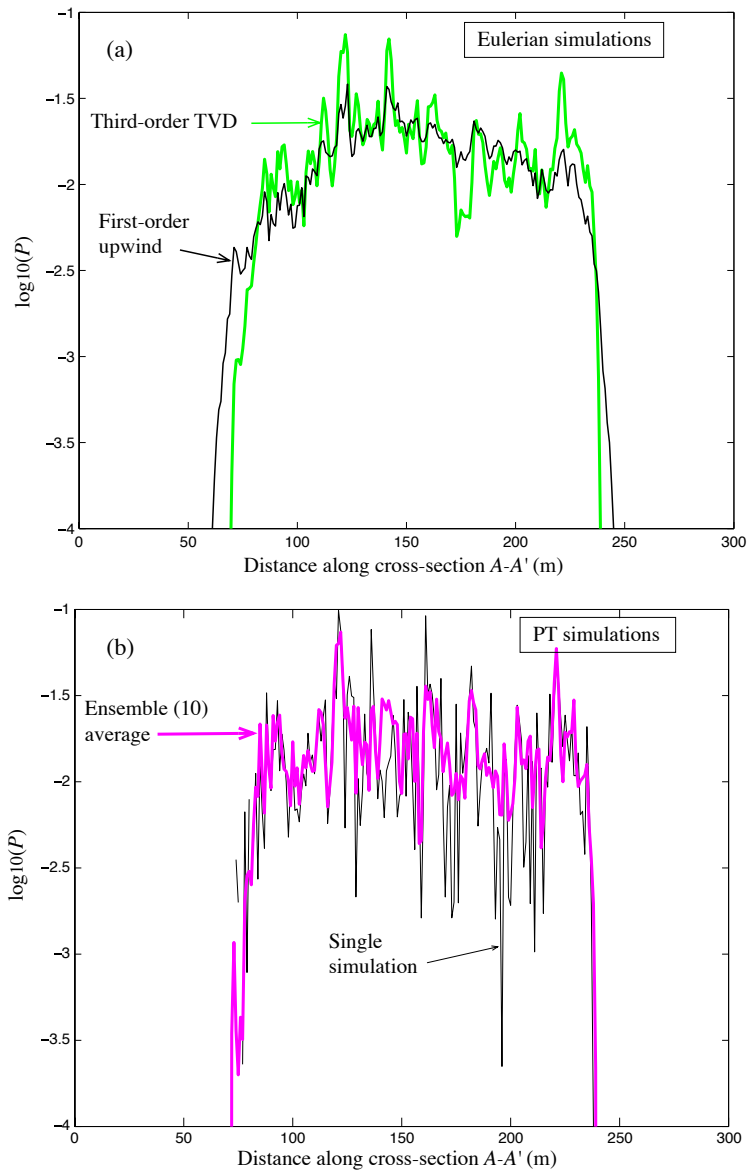


Figure 12: Vertical cross sections $A-A'$ (see Fig. 11) of product concentrations: a) Eulerian simulations, and b) PT simulations—single and ensemble mean of 10 realizations, each with 40,000 particles.

654 executions per node, and K_2 [s] is a small overhead term that accounts for
 655 one-time processes such as initialization of arrays. For the homogeneous
 656 velocity case, the maximum Courant number of unity forces a minimum ex-
 657 ecution time with $K_1 \approx 175$ and 285 for 1st- and 3rd-order algorithms. The
 658 latter takes about 60% longer to run, all things held constant. The PT
 659 simulations are somewhat harder to quantify in the homogeneous velocity
 660 case, because there is no Courant number stability restriction. The particle-
 661 killing algorithm is more efficient in general, and for a range of values of
 662 Δt , it is clear that the computation time increases linearly with $1/\Delta t$ (Fig.
 663 14). The particle-killing algorithm also scales approximately linearly with
 664 the initial number of particles (N), while the particle-number-preserving al-
 665 gorithm scales about linearly with small N but appears to scale with the
 666 (constant-in-time) number of particles to the 1.2 to 1.6th power for larger
 667 numbers (Fig. 14). This is due to the larger number of particles within some
 668 constant search radius given as a multiple of $\sqrt{8D\Delta t}$. For the same reason,
 669 for large particle numbers, decreasing Δt does not cause a linear slowdown
 670 of the particle-preserving method (see the converging computation times for
 671 $\Delta t = 50$ and 10 s in Fig. 14). In other words, because the search becomes
 672 more efficient when the search radius decreases, the cost is lessened when the
 673 timestep is made smaller. Comparing the PT methods to Eulerian, it is clear
 674 that single realizations of either PT method takes less time than the stable
 675 Eulerian methods. Also, achieving better results in the Eulerian methods
 676 by grid refinement is much more taxing than adding particles or changing
 677 timestep size in the PT methods.

678 In the heterogeneous velocity fields, the Eulerian methods still scale with
 679 $T \propto \Delta x^3$ in 2- d , but there is an additional penalty of about $20\times$ due to the
 680 higher maximum velocity in the field. The PT methods also run slower in
 681 the heterogeneous fields, but the penalty is only about $1.3\times$ to $5\times$ because
 682 the Courant number of unity applies to the fastest particle, not the fastest
 683 velocity anywhere in the domain. Because the velocity distribution is highly
 684 skewed (Fig B.3), the maximum particle velocity is far less than the maxi-
 685 mum domain velocity most of the time. Additionally, the number of particles
 686 is a modeler's choice dictated by the heterogeneity of the initial conditions.
 687 Similarly, the choice of is not as restrictive as in the grid-based methods,
 688 so that simulation times for the PT method can be reduced without caus-
 689 ing numerically unstable conditions (unlike the Courant requirement of the
 690 Eulerian models). In theory, *Pollock's* method can be used analytically in
 691 steady flow and semi-analytically in transient flow to determine a particle's

692 advected position over any time interval [79, 71], so the chosen timestep is
693 limited by the diffusion and reaction steps.

694 The reaction step also leads to a particle number stability constraint that
695 arises when dispersion is small: For the particle-number preserving method,
696 the relative change of a particle’s mass when reacting with another particle
697 is maximized when two particles (subscripts 1 and 2) are coincident, and
698 then in $2-d$, $dm_1/m_1 = k_f m_2 / (4\pi \sqrt{\det(\mathbf{D})})$ (see [18]). The values dm_1/m_1
699 should be less than unity, so this can be checked at the start of a simulation
700 when m_2 is largest, and $\det(\mathbf{D})$ is checked at its smallest location. Then the
701 number of particles is increased until m_2 is a small enough number.

702 6. Conclusions

703 The ADRE (1) can be approximated by grid-based or PT algorithms.
704 When the advection error is completely eliminated in homogeneous flow con-
705 ditions, the diffusion and reaction portion of both Eulerian and PT methods
706 converge in an L^1 sense to a “correct” solution. Neither method shows a ten-
707 dency to converge in a pointwise sense given the limitations of desktop-scale
708 computational resources: as Δx is made smaller or the number of particles
709 made larger, the peak concentrations in the domain tend to rise. This point
710 was not exhaustively investigated but has implications for studies concerned
711 with maximum concentrations within a domain.

712 As expected, the errors associated with the approximation of advection
713 dominate the behavior of the grid-based simulations. For displacement of
714 one reactant with another starting with square pulse initial conditions, the
715 errors in a classical 1st-order upwind method are remarkably large. The
716 nonlinear interaction of reactants means that this algorithm would need grid
717 Peclet numbers far less than unity to achieve reasonable solutions in terms of
718 integrated product (i.e., total effective reaction rate). Higher-order methods
719 can have spurious over- or under-mixing, depending on the algorithm and
720 shapes of reactant plumes (Appendix A). The 3rd-order algorithm offers
721 potentially the best balance for current Eulerian methods in use, and appears
722 to require classical grid Peclet numbers $\Delta x/\alpha_L \lesssim 10$ for visually acceptable
723 results in heterogeneous velocity fields. The additional computational cost
724 of the 3rd-order method over simple upwind weighting is about 60%, which is
725 certainly justified for the additional accuracy. Quantitatively, when moving
726 from homogeneous to heterogeneous velocities (all other things held equal
727 with a constant \mathbf{D}) the 3rd-order algorithm produced too much product by

Homogeneous velocity, $D = 0.001I$							
Eulerian				Lagrangian			
Δx	Δt	<i>1st-order upwind</i>	<i>3rd-order TVD</i>	N	Δt	<i>Particle-killing</i>	<i>Particle-preserving</i>
0.49	15	1500	2390	40000	50	170	560
0.98	30	190	332	20000	50	83	187
1.96	60	27	48	10000	50	43	74
				5000	50	23	32
				40000	10	780	1207
				20000	10	387	498
				10000	10	195	209
				5000	10	104	105
Heterogeneous velocity, $\alpha_L = 0.098m; \alpha_T = 0.0098m$							
Eulerian				Lagrangian			
Δx	Δt	<i>1st-order upwind</i>	<i>3rd-order TVD</i>	N	Δt	<i>Particle-killing</i>	<i>Particle-preserving</i>
0.98	1.33	4106	6669	40000	varies	935	1650
				20000	O(5-10)	472	684
				10000		245	320
				5000		140	173

Figure 13: Execution times (seconds) for Eulerian and PT simulations using uniform, isotropic and heterogeneous, anisotropic dispersion. All Eulerian simulations and PT simulations in heterogeneous velocity use a maximum Courant number of unity. Shaded rows highlight approximately similar solutions in the $\lambda = 1$ homogeneous velocity case.

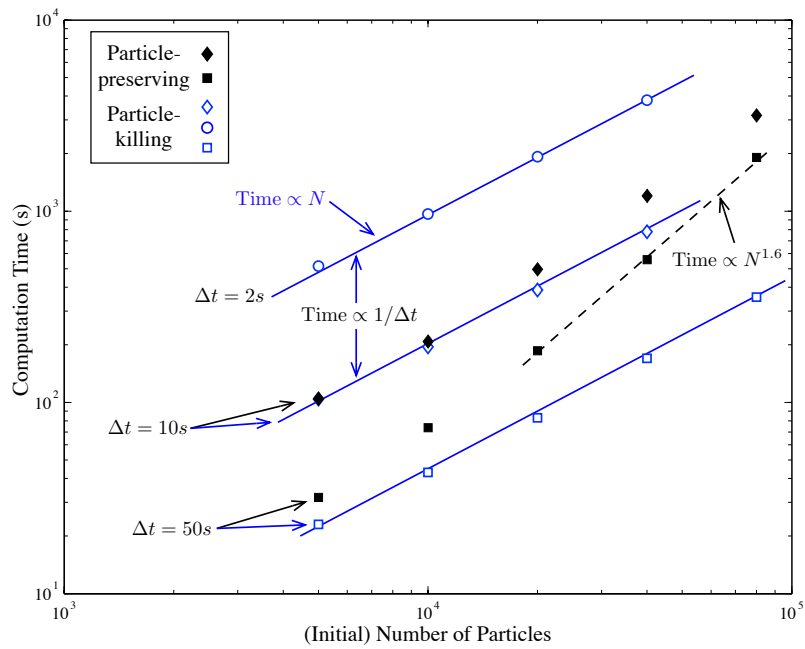


Figure 14: Execution times for PT simulations for different particle numbers and timestep sizes (symbols) and best-fit lines. Particle-killing simulations (open symbols) scale linearly with initial particle numbers; Particle-preserving algorithm scales with $N^{1.7}$. Both scale with $1/\Delta t$.

728 about 2% percent (going from 22.1% to 39.4%) relative to PT methods (from
 729 22.1% to 37.3%). This increased reaction due to fluid deformation (17.3%
 730 versus 15.2%) is too great by a factor of 1.14. The grid-based advection error
 731 has several interesting effects, including increased volume of reaction, large
 732 areas of negative concentrations, and depletion of reactants so that product
 733 cannot be formed farther downstream.

734 The PT methods, whether particle-killing or preserving, have very sim-
 735 ilar amounts of product produced realization to realization, although the
 736 peaks and valleys within single realizations are more pronounced due to the
 737 interplay of fluid deformation and concentration fluctuations. Computationally,
 738 the particle-killing PT method is, in general, much faster than the grid-
 739 based methods for comparable conditions. The particle-preserving algorithm
 740 is also faster, but not drastically so, compared to the Eulerian methods. The
 741 particle-preserving method is more accurate than any of the studied algo-
 742 rithms, particularly at lower concentrations, and requires fewer realizations
 743 to get an estimate of the ensemble average. If initial conditions are known ex-
 744 actly and deterministically, only one Eulerian run is required, so an advantage
 745 is found there. It is impossible to directly compare computation times for Eu-
 746 lerian and PT methods, but the former scales with Δx^{d+1} , and the latter with
 747 $N/\Delta t$ (particle-killing) to $N^1/\Delta t$ to $N^{1.7}/\Delta t$ (particle-preserving). A new
 748 criterion for timestep size $0.25 < 2\sqrt{(8D_m\Delta t)(N(t)/A)} < 3/2$ is proposed
 749 (for 2- d), assuming isotropic diffusion. Time steps falling within this range
 750 permit enough diffusion to allow sufficiently high collision probabilities while
 751 limiting long range, diffusive jumps for a given particle. Additionally, we find
 752 that the particle-preserving methods requires that $1 > k_f m_p / (4\pi \sqrt{\det(\mathbf{D})})$,
 753 where m_p is the initial particle mass.

754 Because of the lack of advection error and favorable computation times,
 755 the PT method can be used to examine the subtle changes to local reaction
 756 rates that arise in heterogeneous flow fields along with spatially heteroge-
 757 neous chemical distributions. At present, the particle methods have only
 758 been extended to relatively simple reaction chains (e.g., Michaelis-Menton
 759 [40]). Based on the advantages of the PT methods, an examination of fur-
 760 ther extensions is warranted.

761 **Appendix A. Review of Finite-Difference Schemes**

762 In multiple dimensions, there are several finite volume/finite difference
 763 algorithms for scalar transport (see, e.g., [98]). An attractive component of

764 several schemes is the TVD requirement, which eliminates spurious oscilla-
765 tions and is a “single-pass” method. The TVD schemes can be applied in
766 single sequential 1- d sweeps by spatial operator splitting. However, these
767 schemes are 1st-order at best [98]. Other schemes can increase the order
768 of convergence accuracy with varying degrees of computational overhead,
769 such as stricter, smaller Courant number criteria, or predictor-corrector type
770 formulations. *Toro* (2009) provides an excellent overview [98]. Here, for ex-
771 position, we choose the TVD methods and show their optimal behavior in
772 1- d .

773 For concentrations q , the wave equation $q_t = -v \cdot q_x$ has an Euler approxi-
774 mation at the i^{th} location and the n^{th} timestep of $q_i^n = q_i - (\Delta t / \Delta x)(f_{i+1/2} -$
775 $f_{i-1/2})$, where f are the fluxes at cell faces. The lack of superscript implies
776 values from the previous $(n - 1)$ timestep. In the simplest case of
777 uniform positive velocity in 1- d and constant Δx , this simplifies to $q_i^n =$
778 $q_i - (v \Delta t / \Delta x)(q_{i+1/2} - q_{i-1/2})$. A first-order upwind or “donor-cell” scheme
779 uses $q_{i-1/2} = q_{i-1}$. Higher-order methods adjust the flux at a cell face to
780 represent the change in concentration over a timestep. This can be derived
781 in several ways [66, 67], including higher-order estimates of the concentration
782 derivatives or predictor-corrector techniques generally referred to as flux cor-
783 rected transport (FCT) (applications to hydrology problems include [52, 27]).
784 We will not investigate the FCT methods here, focusing instead on the ef-
785 ficient one-step TVD methods. The second-order methods use a (linear)
786 estimate of the slope S_i of the concentration in an upwind cell that leads to a
787 change of flux over the timestep. Then integrating the linear change of con-
788 centration over a timestep gives a new estimate of the upwind concentration

$$q_{i-1/2} = q_{i-1} + S_{i-1}(\Delta x - v \Delta t) / 2 \quad (\text{A.1})$$

$$= q_{i-1} + S_{i-1} \Delta x (1 - \lambda) / 2 \quad (\text{A.2})$$

789 A natural choice of slope $S_{i-1} = (q_i - q_{i-1}) / \Delta x$ gives the Lax-Wendroff
790 scheme. These calculated slopes will be discontinuous and can lead to over-
791 shoot and oscillation, so the amount of allowable flux can be limited according
792 to the values of neighboring slopes. If discontinuities are found, the slopes
793 are adjusted. Replacing $S_{i-1} \Delta x$ in the last equation (A.1) with a general
794 function and the difference in the two surrounding known concentrations
795 $\phi(r_{i-1/2})(q_i - q_{i-1})$ gives the flux-limited form

$$q_{i-1/2} = q_{i-1} + \frac{(1 - \lambda)}{2} \phi(r_{i-1/2})(q_i - q_{i-1}) \quad (\text{A.3})$$

796 where $r_{i-1/2} = (q_{i-1} - q_{i-2}) / (q_i - q_{i-1})$ is a ratio of upstream and down-
797 stream gradients relative to the donor cell $i - 1$. Generalizations to vari-
798 able velocity magnitude and direction are straightforward. For reference,
799 the Lax-Wendroff 2^{nd} -order formula sets $\phi(r) = 1$ and leads to overshoot
800 and oscillation. Various schemes have been developed based on eliminat-
801 ing spurious fluctuations. A common method requires that the total vari-
802 ation of q , given for example by $\int |dq/dx| dx$, must not increase. Given
803 this constraint of total variation diminishment (TVD), and keeping the re-
804 quirement that the solution be second-order accurate, *Sweby* [92] showed
805 that the allowable values of $\phi(r)$ must lie in the shaded area of Figure
806 A.1. Schemes that follow the bottom of the region are the most diffusive;
807 schemes along the top are least (and can be compressive, leading to overly
808 steep shock fronts). The four limiters shown on the plot—Roe’s superbee,
809 (see [92]), Van Leer [100], minmod [83], and Leonard’s 3^{rd} -order [65, 31]
810 —are chosen here to represent the range of behaviors. The first-order up-
811 wind scheme uses $\phi(r) = 0$ and can obviously be coded without looking at
812 three nodal concentrations per face and is faster. The 3^{rd} -order solution ad-
813 justs the form of $\phi(r)$ based on the local value of λ (Fig. A.1) according to
814 $\phi(r, \lambda) = \max[0, \min\{\min(2, 2r), \frac{1}{3}((2 - \lambda) + (1 + \lambda)r)\}]$.

815 For an illustration of the effects of the TVD schemes, the ADRE was
816 coded in 1- d using operator splitting. Parameters were held the same as in
817 Section 4. The number of grid blocks was held at 512, or 1/4 the maximum
818 number used in Section 4, roughly representing equivalent computational
819 effort. For the square-pulse initial condition specified (Fig. 1), the least dif-
820 fusive flux limiter (superbee) is clearly most accurate over the full range of
821 Courant numbers tested (Fig. A.2). Based on this plot, one might assume
822 that the superbee limiter is best; however, its compressive (anti-diffusive)
823 nature is well suited to discontinuous concentrations. Smoother fields are
824 artificially sharpened. To illustrate, a similar initial condition is specified in
825 which equal, but Gaussian-shaped masses of reactants A and B are placed
826 near each other (Fig. A.3). The total product masses are lower at $\lambda = 1$
827 because the centers of A and B mass are farther apart, but it is clear that the
828 superbee limiter is under-predicting the overlap and mixing of the plumes at
829 later times (Fig. A.4). In fact, the reaction for $\lambda = 0.1$ has nearly ceased
830 at the end of the simulation (not shown). Clearly, there is no optimal ad-
831 vection scheme for all types of plumes or mixtures of Courant numbers that
832 will be found in a heterogeneous flow field. It is also important to note
833 that extending the higher-order TVD methods to multiple dimensions is not

834 straightforward. Typically, the higher-order methods are applied sequentially
835 in 1- d sweeps via directional operator-splitting. *LeVeque* [67] notes that any
836 method that is TVD in 2- d is, at most, 1st-order accurate, although some
837 multi-dimensional techniques appear to maintain higher-order accuracy in
838 simultaneous multi-dimensional calculations (e.g., [96, 29]). Performing se-
839 quential 1- d sweeps through a multi-dimensional domain is presently the
840 best technique used in water resource applications (especially within readily-
841 available codes), even though that method does not explicitly account for
842 cross-derivatives that naturally come up in the addition of the higher-order
843 anti-diffusion.

844 **Appendix B. Semi-Analytical Solutions for Mass of Product Pro-** 845 **duced**

846 Solutions are tractable under two end-member conditions: fast and slow
847 reactions.

848 *Appendix B.1. Slow Reaction - A Perturbation Solution Approach*

849 In 1-d the ADRE (1) is given by

$$\frac{\partial C_i}{\partial t} + u \frac{\partial C_i}{\partial x} = D \frac{\partial^2 C_i}{\partial x^2} - k C_A C_B \quad i = A, B \quad (\text{B.1})$$

850 This equation can be rewritten in dimensionless forms by defining dimension-
851 less variables $t^* = t \frac{u}{l}$, $x^* = x/l$, and $C^* = C/C_{ref}$, where l is a characteristic
852 distance (e.g., the initial width of the plume in our simulations) and C_{ref}
853 is a characteristic concentration (e.g., the initial concentration). For ease of
854 notation we drop the stars and in dimensionless form (B.1) becomes

$$\frac{\partial C_i}{\partial t} + \frac{\partial C_i}{\partial x} = \frac{1}{Pe} \frac{\partial^2 C_i}{\partial x^2} - Da C_A C_B \quad i = A, B \quad (\text{B.2})$$

855 where $Pe = \frac{ul}{D}$ is the Peclet number and $Da = \frac{kC_0 l}{u}$ the Damköhler number.
856 We are considering the limit of slow reactions and thus take Da as small.
857 Doing this we can write the following expansion for concentration [99]:

$$C_i = \sum_{n=0}^{\infty} C_i^{(n)} Da^n \quad (\text{B.3})$$

858 Then at $O(Da^0)$

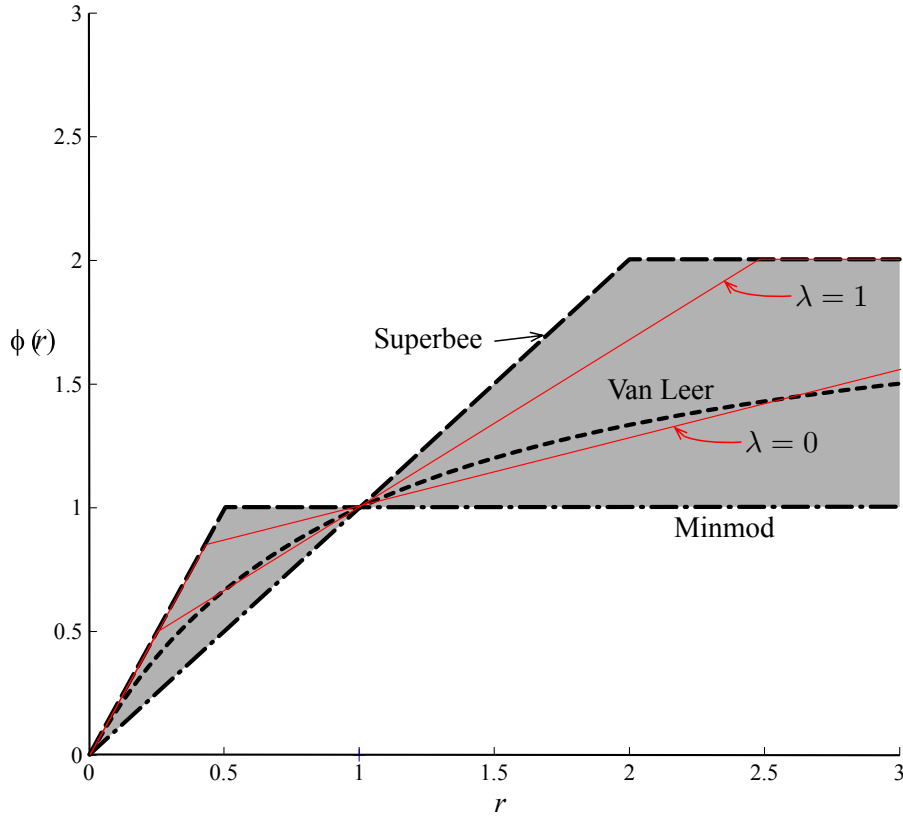


Figure A.1: Region of acceptable TVD flux-limiters [92]. Limiters for this study are the 2^{nd} -order maximally diffusive minmod (dash-dot line), minimally diffusive superbee (large dashes), intermediate Van Leer (small dashes), and Leonard's 3^{rd} -order, which depends on local Courant number and smoothly interpolates the region between $\lambda = [0, 1]$ (red solid lines).

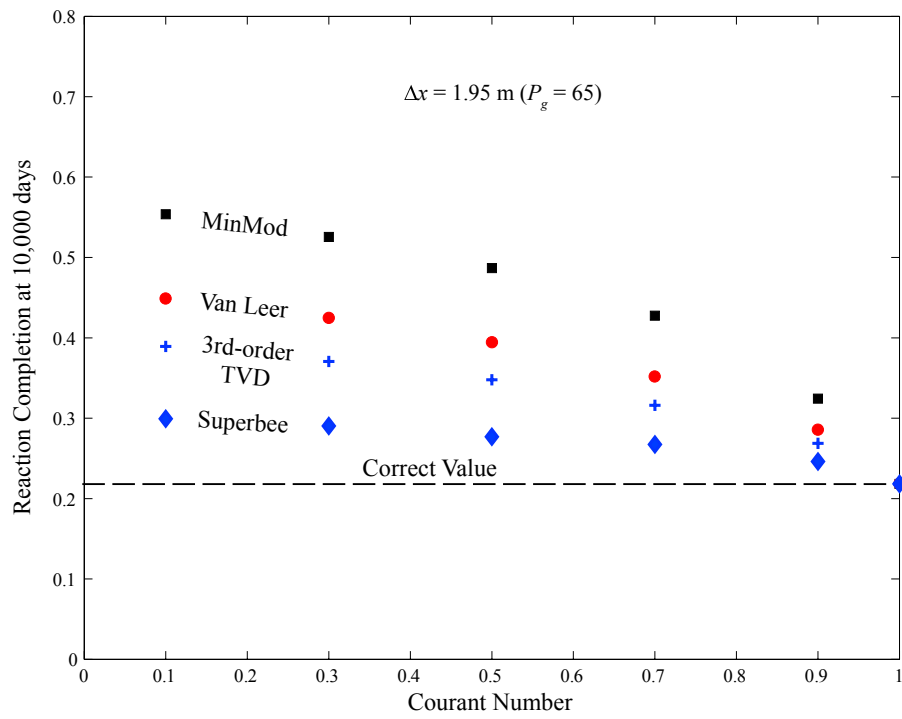


Figure A.2: 1- d solutions to the adjacent square-pulse initial condition problem using different TVD advection schemes.

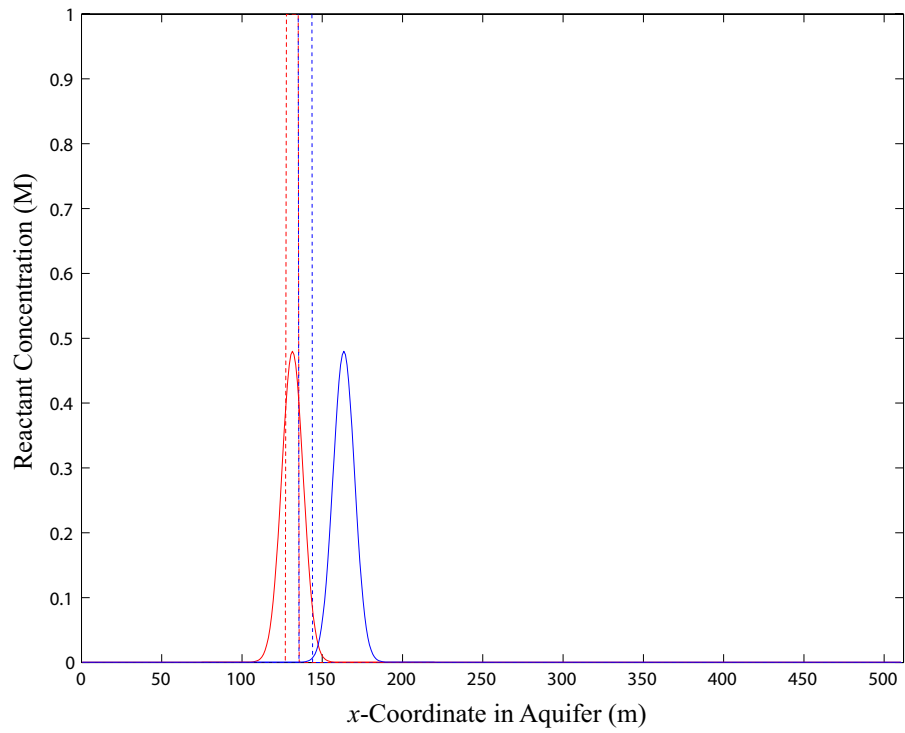


Figure A.3: 1- d versions of the two initial conditions of reactants A (red) and B (blue). The square pulses (dotted) mimic the original 2- d simulations in Section 4. An additional set of I.C.s is shown that place identical masses in nearby Gaussian pulses (solid red and blue curves).

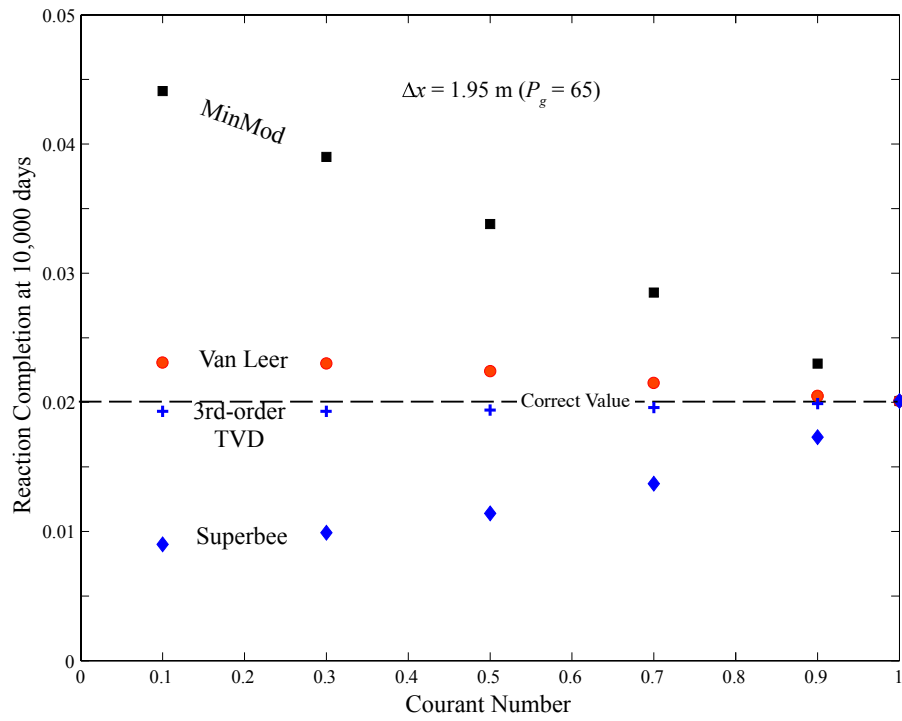


Figure A.4: 1- d solutions to the adjacent Gaussian-pulse initial condition problem using different TVD advection schemes.

$$\frac{\partial C_i^{(0)}}{\partial t} + \frac{\partial C_i^{(0)}}{\partial x} = \frac{1}{Pe} \frac{\partial^2 C_i^{(0)}}{\partial x^2} \quad i = A, B \quad (\text{B.4})$$

859 Recognizing that the effect of advection is just a Gallilean shift, we move
860 into a moving reference frame $z = x - t$ and

$$\frac{\partial C_i^{(0)}}{\partial t} = \frac{1}{Pe} \frac{\partial^2 C_i^{(0)}}{\partial z^2} \quad i = A, B \quad (\text{B.5})$$

861 In an infinite domain the solution to these equations is given by

$$C_i^{(0)} = \sqrt{\frac{Pe}{4\pi t}} \int_{-\infty}^{\infty} e^{-\frac{(z-\xi)^2 Pe}{4t}} C_i(t=0) d\xi \quad (\text{B.6})$$

862 At $O(Da^1)$

$$\frac{\partial C_i^{(1)}}{\partial t} = \frac{1}{Pe} \frac{\partial^2 C_i^{(1)}}{\partial z^2} - C_A^{(0)} C_B^{(0)} \quad i = A, B \quad (\text{B.7})$$

863 Given this equation and truncating series (B.3) for concentrations at $O(Da^1)$
864 the total mass of the product will be given by

$$M(t) = Da \int_{-\infty}^{\infty} \int_0^t C_A^{(0)}(z, t') C_B^{(0)}(z, t') dt' dz \quad (\text{B.8})$$

865 Thus in principle for any initial condition we can now calculate the pro-
866 duced mass to within approximation of the perturbation series. Any error
867 introduced via numerical dispersion will manifest as an error in the concentra-
868 tion fields $C_A^{(0)}(z, t')$ and $C_B^{(0)}(z, t')$ via a modified $Pe = (ul)/(D + D_{numerical})$,
869 which will compound in an error in the resultant product mass.

870 The nonlinear and initial condition specific nature of the reaction makes
871 it difficult to make general statements on how this error will manifest. For
872 demonstration purposes, consider the following simple example, an infinite
873 domain half filled with A and half filled with B , separated by a sharp interface
874 at $x = 0$. At short times (i.e., when the diffusive length is much less than
875 the initial plume width) this mimics the example setups studied in this work.
876 For this setup the initial conditions are given by

$$\begin{aligned} C_A(t=0) &= 1 & -\infty < x < 0 \\ C_B(t=0) &= 1 & 0 < x < \infty \end{aligned} \quad (\text{B.9})$$

877 and zero elsewhere, which means

$$C_A^{(0)}(z, t) = \frac{1}{2} \operatorname{erfc} \left[\frac{z\sqrt{Pe}}{\sqrt{4t}} \right] \quad C_B^{(0)}(z, t) = 1 - \frac{1}{2} \operatorname{erfc} \left[\frac{z\sqrt{Pe}}{\sqrt{4t}} \right] \quad (\text{B.10})$$

878 Thus solving (B.8) is trivial and gives

$$M(t) = \frac{2}{3} Da \sqrt{\frac{2}{\pi Pe}} t^{3/2} \quad (\text{B.11})$$

879 The key feature is that $M(t) \propto \frac{1}{\sqrt{Pe}}$, or in dimensional terms that the
 880 mass or product produced is proportional to \sqrt{D} . Given that in the Eulerian
 881 numerical models the dispersion coefficient will be $D = D_{actual} + D_{numerical}$,
 882 any error in the dispersion coefficient induced by numerical dispersion will
 883 increase the predicted amount of mass produced in this manner. The results
 884 for the specific initial conditions studied in this paper are cumbersome and
 885 provide little insight and are thus not shown. However, to leading order it
 886 can be shown that the initial condition studied in this paper has the same
 887 scaling.

888 *Appendix B.2. Fast Reactions*

889 Now if we consider the other extreme when Da is large, we can treat the
 890 reaction as instantaneous, which in previous studies has been shown to be a
 891 good assumption for $Da > 10$ [86]. Under this assumption A and B cannot
 892 coexist, meaning that the lesser will be consumed entirely. Now following the
 893 development of *Gramling et al.* (2002) [47], define two conservative pseudo-
 894 tracers as

$$U_A = C_A + C_P \quad U_B = C_B + C_P \quad (\text{B.12})$$

895 These are governed by a conservative transport equation because upon
 896 summation of the ADREs (1) for C_A and C_P , the reaction terms disappear
 897 (because A and B disappear at the same rate as P by stoichiometry). For
 898 the initial conditions considered in B.1

$$\begin{aligned} U_A(t=0) &= 1 & -\infty < x < 0 \\ U_B(t=0) &= 1 & 0 < x < \infty \end{aligned} \quad (\text{B.13})$$

899 which means that at all times

$$U_A(t) = \frac{1}{2} \operatorname{erfc} \left[\frac{(x - ut)\sqrt{Pe}}{\sqrt{4t}} \right] \quad U_B(t) = 1 - \frac{1}{2} \operatorname{erfc} \left[\frac{(x - ut)\sqrt{Pe}}{\sqrt{4t}} \right] \quad (\text{B.14})$$

900 Now since A and B cannot coexist, the concentration of product is given by

$$C_P = \min(U_A, U_B) \quad (\text{B.15})$$

901 and the total mass of product for the semi-infinite sources (following [47]) is
902 given by

$$M = \int_{-\infty}^{\infty} C_P dx = 2 \int_0^{\infty} U_A dx = 2\sqrt{\frac{t}{Pe\pi}} \quad (\text{B.16})$$

903 A more accurate equation for the finite (in the x -direction) sources is

$$M_C(t) = \sqrt{\frac{4t}{\pi Pe}} \left(1 - e^{-\frac{Pe}{4t}} \right) + 1 - \operatorname{erf} \left[\sqrt{\frac{Pe}{4t}} \right] \quad (\text{B.17})$$

904 which recovers (B.16) for $l \rightarrow \infty$. The 20,000 particle simulations follow
905 formula (B.17) fairly closely at later time (Fig. B.1) using the initial condition
906 $l = 15.6$ m for an estimation of the scaling length. The early time discrepancy
907 is most likely due to the fact that our reactions are not instantaneous, but
908 take some time (albeit small) to develop.

909 *Appendix B.3. Slow reactions generalized to a higher order reaction $-kC_A^n C_B^m$*

910 To demonstrate how these effect might be influenced for higher order
911 reactions, consider taking $r = -kC_A^n C_B^m$. Following the same procedures as
912 above for slow reactions (i.e. Appendix B.1) the total mass produced will be

$$M(t) = \int_0^t \int_{-\infty}^{\infty} Da \frac{Pe^{\frac{n+m}{2}}}{(4\pi t')^{\frac{n+m}{2}}} \prod_{i=1}^n \int_{-\infty}^0 e^{-\frac{(x-\xi_i)^2 Pe}{4t'}} d\xi_i \prod_{j=1}^m \int_0^{\infty} e^{-\frac{(x-\eta_j)^2 Pe}{4t'}} d\eta_j dx dt' \quad (\text{B.18})$$

913 Now rescale all the length scales by $\sqrt{\frac{Pe}{4t'}}$, i.e.

$$\xi' = \xi \sqrt{\frac{Pe}{4t'}} \quad \eta' = \eta \sqrt{\frac{Pe}{4t'}} \quad x = x \sqrt{\frac{Pe}{4t'}} \quad (\text{B.19})$$

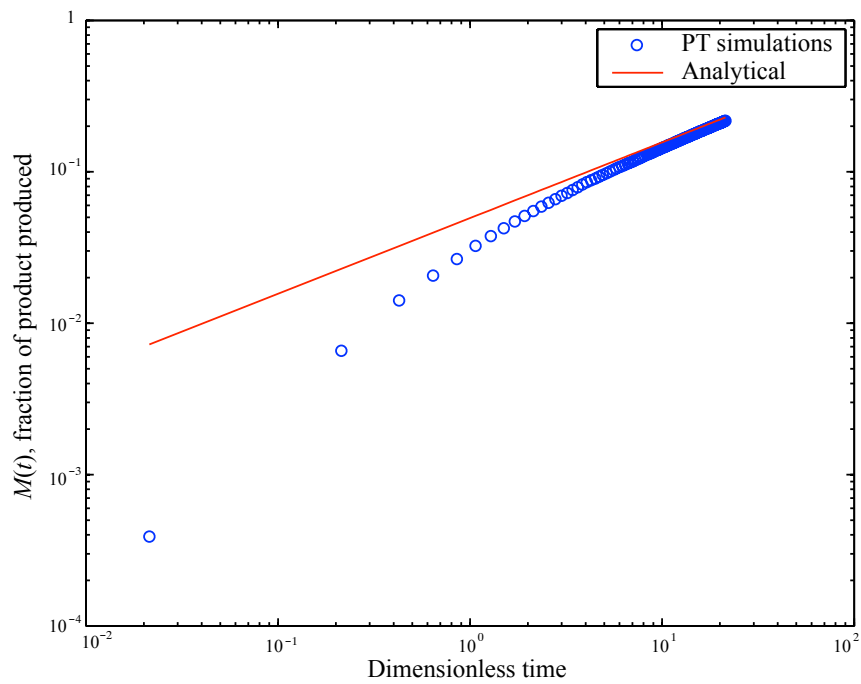


Figure B.1: Evolution of the mass of product in the 20,000 particle simulations in a homogeneous velocity field (symbols), along with the solution to the analytical expression (B.17).

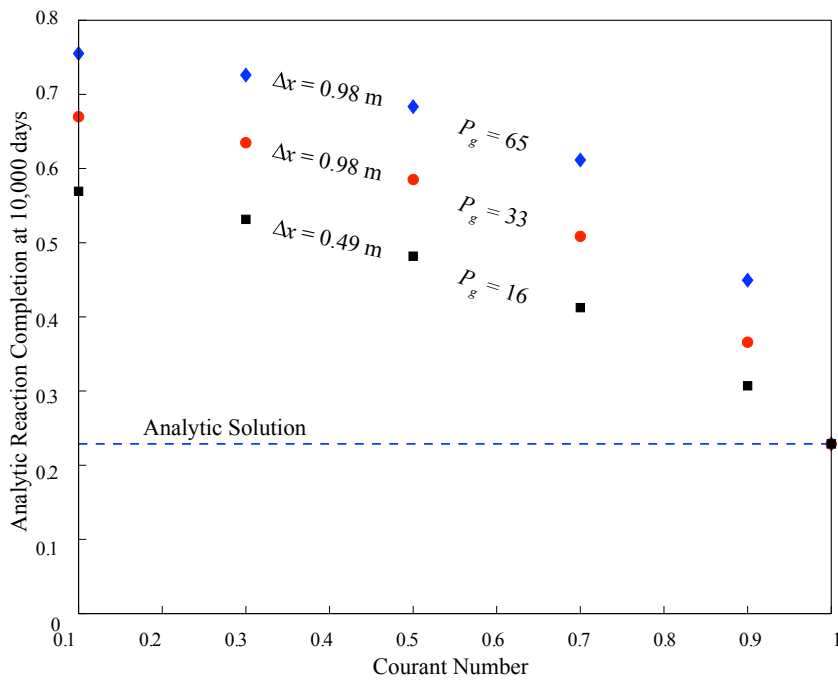


Figure B.2: Analytic solutions (using (B.17)) for mass created at 10,000 days incorporating the errors due to numerical dispersion for the upwind scheme.

914 Then

$$M(t) = \int_0^t \int_{-\infty}^{\infty} Da \sqrt{\frac{4t'}{Pe}} \frac{1}{\pi^{\frac{n+m}{2}}} \prod_{i=1}^n \int_{-\infty}^0 e^{-(x-\xi_i)^2} d\xi_i \prod_{j=1}^m \int_0^{\infty} e^{-(x-\eta_j)^2} d\eta_j dx dt' \quad (\text{B.20})$$

915 which gives

$$M(t) = W \frac{2Da}{3} \sqrt{\frac{2}{Pe}} t^{3/2} \quad (\text{B.21})$$

916 where the constant W is given by

$$W = \frac{1}{\pi^{\frac{n+m}{2}}} \int_{-\infty}^{\infty} \prod_{i=1}^n \int_{-\infty}^0 e^{-(x-\xi_i)^2} d\xi_i \prod_{j=1}^m \int_0^{\infty} e^{-(x-\eta_j)^2} d\eta_j dx \quad (\text{B.22})$$

917 The specific value of W is unimportant to the central message. From
 918 (B.21) we see again that the total amount of mass produced has the same
 919 proportionality as before of $M(t) \propto \frac{1}{\sqrt{Pe}}$. At this point it is not clear how to
 920 generalize the fast reactions scenario to higher order reactions.

921 *Appendix B.4. Error Estimates*

922 The foregoing sections of this Appendix show that the mass produced is
 923 roughly proportional to \sqrt{D} . This allows the construction of some rules-of-
 924 thumb for error estimation. The ratio of mass produced with numerical error
 925 to mass produced without error is $\sqrt{D_{actual} + D_{numerical}} / \sqrt{D_{actual}}$. Therefore
 926 the excess amount of mass produced in error expressed as a fraction of the
 927 real amount is $Error = \sqrt{1 + D_{numerical}/D_{actual}} - 1$. For isotropic, fixed
 928 D_{actual} in our first-order upwind scheme, we have

$$Error = \sqrt{1 + \frac{|v|\Delta x}{2D_{actual}}(1 - |v|\Delta t/\Delta x)} - 1 \quad (\text{B.23})$$

929 In the case of velocity-dependent dispersion in which the longitudinal disper-
 930 sion is given by $D_{actual} = \alpha_L |v|$, the error is

$$Error = \sqrt{1 + \frac{\Delta x}{2\alpha_L}(1 - |v|\Delta t/\Delta x)} - 1 \quad (\text{B.24})$$

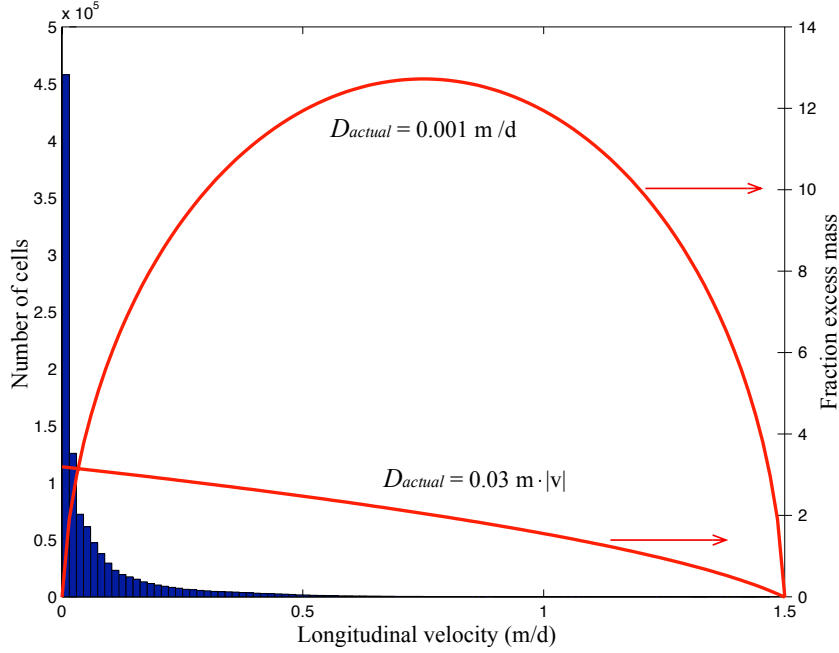


Figure B.3: Histogram (blue bars) of velocity magnitude in the heterogeneous domain pictured in Fig 8. Estimates of the excess mass production error (red curves) by the upwind advection algorithm as a function of velocity (hence grid Peclet and Courant numbers) for fixed dispersion value $0.001 \text{ m}^2/\text{d}$ and a velocity-dependent dispersion with $\alpha_L = 0.03 \text{ m}$. The right-hand labels are for excess error as a multiple of the real production value.

931 The latter of these two errors is greater for regions of smaller velocity in
 932 the domain, as the former goes to zero for $|v| \rightarrow 0$. Figure B.3 shows the
 933 magnitude of these two error estimates for reasonable values in the exam-
 934 ple heterogeneous domain ($\Delta x = 1 \text{ m}$, $\max(v) = 1.46 \text{ m/d}$), along with
 935 a histogram of the velocities within the (log-normal) K field. For a large
 936 portion of the domain experiencing low velocity, the error is greater for a
 937 velocity-dependent dispersion.

938 **Appendix C. PT simulation of anisotropic dispersion and reaction.**

939 We solve (1) via PT using operator-splitting as follows: The finite-time
 940 discretized Langevin equation applied to each particle's position \mathbf{X} for the
 941 backward Kolmogorov transport portion of equation (1) follows $\mathbf{X}_{t+\Delta t} =$

942 $\mathbf{X}_t + (\mathbf{v} + \nabla \mathbf{D})\Delta t + \mathbf{B}W$, where $\mathbf{B} = \sqrt{2\Delta t \mathbf{D}}$ after \mathbf{D} is diagonalized
 943 by rotation into a coordinate system along the flow direction, and W is a
 944 standard multiGaussian random vector [60].

945 The velocities are calculated at cell faces following an iterative solution of
 946 the continuity equation for constant-density fluid $\nabla \cdot K \nabla h = 0$ followed by
 947 $\mathbf{v} = -K \nabla h / \theta$. Constant values of h at the left and right boundaries, along
 948 with no-flow $\nabla h \cdot \mathbf{n} = 0$ along the top and bottom boundaries maintain
 949 the desired mean gradient from left to right. The K is constant within
 950 each rectilinear volume (cell), porosity θ is constant everywhere, and \mathbf{v} is
 951 calculated at cell faces and linearly interpolated to each particle's location
 952 within the cells. Dispersion components for each particle use these linearly-
 953 interpolated velocities. Because the calculation of the gradients of dispersion
 954 coefficients at the exact particle location are relatively time consuming by
 955 bilinear interpolation (see [60]), we make a simplification that the gradients
 956 can be well approximated as constant within each cell. This follows directly
 957 from the linear velocity interpolation and linear dispersion dependence on
 958 velocity. For example, in 2- d with indices i, j in the x, y -directions, the
 959 components D_{xx} and D_{yx} are calculated at the $i - 1/2$ and $i + 1/2$ faces,
 960 while D_{yy} and D_{xy} are calculated at the $j - 1/2$ and $j + 1/2$ faces. So for
 961 the i, j block, $\frac{dD_{xx}}{dx} = (D_{xx}(i + 1/2) - D_{xx}(i - 1/2))/\Delta x$, $\frac{dD_{yx}}{dx} = (D_{yx}(i +$
 962 $1/2) - D_{yx}(i - 1/2))/\Delta x$, $\frac{dD_{yy}}{dy} = (D_{yy}(j + 1/2) - D_{yy}(j - 1/2))/\Delta y$, $\frac{dD_{xy}}{dy} =$
 963 $(D_{xy}(j + 1/2) - D_{xy}(j - 1/2))/\Delta y$.

964 In the operator-split method, we enforce zero-diffusive flux BCs in the
 965 random walk by reflecting all particles back into the domain [e.g., 85]. Par-
 966 ticles that move by advection into boundary cells are removed, enforcing
 967 $J = \mathbf{n} \cdot \mathbf{v}C$, where \mathbf{n} is the unit normal to the boundary and the relation of
 968 concentration to particle mass is thought of as the spatial convolution of any
 969 particle's mass with some kernel function with unit integral in d -dimensions.
 970 A nice discussion of all types of boundary conditions for advection and dis-
 971 persion via the PT method is given by *Koch and Nowak* [58].

972 Reactions between particles may either follow the formulas given in [11]
 973 or [18] for particle-killing or particle-preserving methods, respectively. For
 974 the latter, each A particle with unique mass $m_A(t)$ at time t is chosen
 975 and sequentially subjected to reaction with nearby B particles with unique
 976 mass m_B . The change in masses for a single reaction are $dm_A = dm_B =$
 977 $-\Delta t k_f m_B(t) m_A(t) v(\mathbf{s})$. Then the net change sums over all reaction partner
 978 pairs $m_A(t + \Delta t) = m_A(t) + \sum dm_A$. The co-location density $v(\mathbf{s})$ given a

979 separation vector \mathbf{s} between an A and B particle pair is given by a multi-
980 Gaussian

$$v(\mathbf{s}) = \frac{1}{(8\pi\Delta t)^{d/2}|\mathbf{D}|^{1/2}} \exp\left(-\frac{1}{8\Delta t}\mathbf{s}'\mathbf{D}^{-1}\mathbf{s}\right). \quad (\text{C.1})$$

981 The search radius for nearby particles was restricted to $3\sqrt{8\max(D_{ij})\Delta t}$, and
982 the kd-tree algorithm [14] for nearby particle searching was used as coded in
983 the “rangesearch” algorithm in matlab.

984 We assume, for calculation speed, that the dispersion tensor is simply that
985 of the “central” A particle. The differences in dispersion tensors between the
986 A and each nearby B particle was ignored, i.e., $\mathbf{D} = \mathbf{D}_A$. For isotropic
987 dispersion, the above procedure was used with $\mathbf{D} = D\mathbf{I}$.

- 988 [1] Apello, C. A. J., Postma, D., 2005. *Geochemistry, Groundwater and*
989 *Pollution*, 2nd Edition. CRC Press.
- 990 [2] Audigane, P., Gaus, I., Czernichowski-Lauriol, I., Pruess, K., Xu, T.,
991 2007. Two-dimensional reactive transport modeling of CO₂ injection
992 in a saline aquifer at the Sleipner site, North Sea. *Am. J. Sci.* 307 (7),
993 974–1008.
994 URL <http://www.ajsonline.org/cgi/content/abstract/307/7/974>
- 995 [3] Avesani, D., Herrera, P., Chiogna, G., Bellin, A., Dumbser, M., 6 2015.
996 Smooth particle hydrodynamics with nonlinear moving-least-squares
997 weno reconstruction to model anisotropic dispersion in porous media.
998 *Advances in Water Resources* 80 (0), 43–59.
999 URL <http://www.sciencedirect.com/science/article/pii/S0309170815000627>
- 1000 [4] Ayuso, B., Marini, L. D., 2009. Discontinuous Galerkin methods for
1001 advection-diffusion-reaction problems. *SIAM J. Numer. Anal.* 47 (2),
1002 1391–1420.
- 1003 [5] Bakker, M., Hemker, K., 2004. Analytic solutions for groundwater
1004 whirls in box-shaped, layered anisotropic aquifers. *Advances in Water*
1005 *Resources* 27 (11), 1075–1086.
1006 URL <http://www.sciencedirect.com/science/article/pii/S0309170804001344>
- 1007 [6] Barry, D., Prommer, H., Miller, C., Engesgaard, P., Brun, A., Zheng,
1008 C., 2002. Modelling the fate of oxidisable organic contaminants in
1009 groundwater. *Advances in Water Resources* 25 (8–12), 945 – 983.
1010 URL <http://www.sciencedirect.com/science/article/pii/S0309170802000441>

- 1011 [7] Battiato, I., Tartakovsky, D. M., 2011. Applicability regimes for macro-
1012 scopic models of reactive transport in porous media. *J. Contam. Hydrol.*
1013 120-121, 18–26.
- 1014 [8] Battiato, I., Tartakovsky, D. M., Tartakovsky, A. M., Scheibe, T., 2009.
1015 On breakdown of macroscopic models of mixing-controlled heteroge-
1016 neous reactions in porous media. *Adv. Water Resour.* 32, 1664–1673.
- 1017 [9] Bechtold, M., Vanderborght, J., Ippisch, O., Vereecken, H., 2011. Effi-
1018 cient random walk particle tracking algorithm for advective-dispersive
1019 transport in media with discontinuous dispersion coefficients and water
1020 contents. *Water Resour. Res.* 47 (10), W10526–.
1021 URL <http://dx.doi.org/10.1029/2010WR010267>
- 1022 [10] Benson, D. A., Carey, A. E., Wheatcraft, S. W., 1998. Numerical ad-
1023 vective flux in highly variable velocity fields exemplified by saltwater
1024 intrusion. *J. Contam. Hydrol.* 34, 207–233.
- 1025 [11] Benson, D. A., Meerschaert, M. M., Dec. 2008. Simulation of chemical
1026 reaction via particle tracking: Diffusion-limited versus thermodynamic
1027 rate-limited regimes. *Water Resour. Res.* 44, W12201.
1028 URL <http://dx.doi.org/10.1029/2008WR007111>
- 1029 [12] Benson, D. A., Meerschaert, M. M., 2009. A simple and efficient ran-
1030 dom walk solution of multi-rate mobile/immobile mass transport equa-
1031 tions. *Adv. Water Resour.* 32, 532–539.
- 1032 [13] Benson, D. A., Meerschaert, M. M., Revielle, J., Jan. 2013. Fractional
1033 calculus in hydrologic modeling: A numerical perspective. *Advances*
1034 *in Water Resources* 51 (0), 479–497.
1035 URL <http://www.sciencedirect.com/science/article/pii/S0309170812000899>
- 1036 [14] Bentley, J. L., 1975. Multidimensional binary search trees used for as-
1037 sociative searching. *Communications of the Association for Computing*
1038 *Machinery* 18, 509–517.
- 1039 [15] Bokanowski, O., Zidani, H., 2007. Anti-dissipative schemes for advec-
1040 tion and application to Hamilton–Jacobi–Bellmann equations 30 (1),
1041 1–33–.
1042 URL <http://dx.doi.org/10.1007/s10915-005-9017-0>

- 1043 [16] Bolster, D., de Anna, P., Benson, D. A., Tartakovsky, A. M., 2012.
1044 Incomplete mixing and reactions with fractional dispersion. *Advances*
1045 *in Water Resources* 37, 86–93.
- 1046 [17] Bolster, D., Dentz, M., Borgne, T. L., 2011. Hyper mixing in shear
1047 flow. *Water Resources Research* 47, W09602.
- 1048 [18] Bolster, D., Paster, A., Benson, D. A., 2016. A particle number con-
1049 serving Lagrangian method for mixing-driven reactive transport. *Water*
1050 *Resources Research* 52 (2), 1518–1527.
1051 URL <http://dx.doi.org/10.1002/2015WR018310>
- 1052 [19] Bolster, D., Valdés-Parada, F. J., LeBorgne, T., Dentz, M., Carrera,
1053 J., 2011. Mixing in confined stratified aquifers. *Journal of Contaminant*
1054 *Hydrology* 120, 198–212.
- 1055 [20] Boso, F., Bellin, A., Dumbser, M., 2013. Numerical simulations of so-
1056 lute transport in highly heterogeneous formations: A comparison of
1057 alternative numerical schemes. *Advances in Water Resources* 52, 178–
1058 189.
- 1059 [21] Burchard, H., Rennau, H., 2008. Comparative quantification of
1060 physically and numerically induced mixing in ocean models. *Ocean*
1061 *Modelling* 20 (3), 293–311.
1062 URL <http://www.sciencedirect.com/science/article/pii/S146350030700128X>
- 1063 [22] Chakraborty, P., Meerschaert, M. M., Lim, C. Y., 2009. Parameter es-
1064 timation for fractional transport: A particle-tracking approach. *Water*
1065 *Resour. Res.* 45 (10), W10415–.
1066 URL <http://dx.doi.org/10.1029/2008WR007577>
- 1067 [23] Chiogna, G., Bellin, A., 2013. Analytical solution for reactive solute
1068 transport considering incomplete mixing within a reference elementary
1069 volume. *Water Resources Research* 49 (5), 2589–2600.
1070 URL <http://dx.doi.org/10.1002/wrcr.20200>
- 1071 [24] Chiogna, G., Hochstetler, D. L., Bellin, A., Kitanidis, P. K., Rolle,
1072 M., 2012. Mixing, entropy and reactive solute transport. *Geophysical*
1073 *Research Letters* 39 (20).

- 1074 [25] Chiogna, G., Rolle, M., Bellin, A., Cirpka, O. A., Nov. 2014. Helicity
1075 and flow topology in three-dimensional anisotropic porous media.
1076 *Advances in Water Resources* 73 (0), 134–143.
1077 URL <http://www.sciencedirect.com/science/article/pii/S0309170814001341>
- 1078 [26] Cirpka, O. A., de Barros, F. P. J., Chiogna, G., Rolle, M., Nowak, W.,
1079 Jun. 2011. Stochastic flux-related analysis of transverse mixing in two-
1080 dimensional heterogeneous porous media. *Water Resour. Res.* 47 (6),
1081 W06515–.
- 1082 [27] Cirpka, O. A., Frind, E. O., Helmig, R., 1999. Numerical methods
1083 for reactive transport on rectangular and streamline-oriented grids.
1084 *Advances in Water Resources* 22 (7), 711 – 728.
1085 URL <http://www.sciencedirect.com/science/article/pii/S0309170898000517>
- 1086 [28] Cockburn, B., Shu, C., 1998. The local discontinuous Galerkin method
1087 for time-dependent convection-diffusion systems. *SIAM Journal on Nu-
1088 merical Analysis* 35 (6), 2440–2463.
- 1089 [29] Colella, P., Mar. 1990. Multidimensional upwind methods for hyper-
1090 bolic conservation laws. *Journal of Computational Physics* 87 (1),
1091 171–200.
1092 URL <http://www.sciencedirect.com/science/article/pii/002199919090233Q>
- 1093 [30] Constantinescu, E. M., Sandu, A., Carmichael, G. R., 2008. Modeling
1094 atmospheric chemistry and transport with dynamic adaptive resolu-
1095 tion. *Computational Geosciences* 12 (2), 133–151.
1096 URL <http://dx.doi.org/10.1007/s10596-007-9065-7>
- 1097 [31] Datta-Gupta, A., Lake, L. W., Pope, G. A., Sephernoori, K., King,
1098 M. J., 1991. High-resolution monotonic schemes for reservoir fluid flow
1099 simulation. *In Situ*, 289–317.
- 1100 [32] de Anna, P., Dentz, M., Tartakovsky, A., Le Borgne, T., 2014. Fila-
1101 mentary structure of mixing fronts controls reaction kinetics in porous
1102 media flows. *Geophysical Research Letters*, in press.
- 1103 [33] de Anna, P., Jimenez-Martinez, J., Tabuteau, H., Turuban, R.,
1104 Le Borgne, T., Derrien, M., Méheust, Y., 2013. Mixing and reaction
1105 kinetics in porous media: an experimental pore scale quantification.
1106 *Environmental Science & Technology* 48 (1), 508–516.

- 1107 [34] de Barros, F. P., Dentz, M., 2016. Pictures of blockscale transport:
1108 Effective versus ensemble dispersion and its uncertainty. *Advances in*
1109 *Water Resources* 91, 11 – 22.
1110 URL <http://www.sciencedirect.com/science/article/pii/S0309170816300549>
- 1111 [35] de Barros, F. P. J., Dentz, M., Kock, J., Nowak, W., 2012. Flow topol-
1112 ogy and scalar mixing in spatially heterogeneous flow fields. *Geophys.*
1113 *Res. Lett.* 39, L08404.
- 1114 [36] De Simoni, M., Carrera, J., Sanchez-Vila, X., Guadagnini, A., 2005. A
1115 procedure for the solution of multicomponent reactive transport prob-
1116 lems. *Water Resources Research* 41 (11).
- 1117 [37] De Simoni, M., Sanchez-Vila, X., Carrera, J., Saaltink, M., 2007. A
1118 mixing ratios-based formulation for multicomponent reactive transport.
1119 *Water Resources Research* 43 (7).
- 1120 [38] Dentz, M., Le Borgne, T., Englert, A., Bijeljic, B., 2011. Mixing,
1121 spreading and reaction in heterogeneous media: A brief review. *Journal*
1122 *of Contaminant Hydrology* 120, 1–17.
- 1123 [39] Ding, D., Benson, D., Paster, A., Bolster, D., 2012. Modeling bimolec-
1124 ular reactions and transport in porous media via particle tracking. *Ad-*
1125 *vances in Water Resources* 53, 56–65.
- 1126 [40] Ding, D., Benson, D. A., 2015. Simulating biodegradation under
1127 mixing-limited conditions using michaelis–menten (monod) kinetic
1128 expressions in a particle tracking model. *Advances in Water Resources*
1129 76, 109 – 119.
1130 URL <http://www.sciencedirect.com/science/article/pii/S0309170814002462>
- 1131 [41] Doi, M., 1976. Stochastic theory of diffusion-controlled reaction. *Jour-*
1132 *nal of Physics A: Mathematical and General* 9, 1479–1495.
- 1133 [42] Edery, Y., Scher, H., Berkowitz, B., Jan. 2009. Modeling bimolecular
1134 reactions and transport in porous media. *Geophys. Res. Lett.* 36 (2),
1135 L02407.
1136 URL <http://dx.doi.org/10.1029/2008GL036381>

- 1137 [43] Engdahl, N. B., Benson, D. A., Bolster, D., Nov 2014. Predicting the
1138 enhancement of mixing-driven reactions in nonuniform flows using mea-
1139 sures of flow topology. *Phys. Rev. E* 90, 051001.
1140 URL <http://link.aps.org/doi/10.1103/PhysRevE.90.051001>
- 1141 [44] Fernàndez-Garcia, D., Sanchez-Vila, X., 2011. Optimal reconstruction
1142 of concentrations, gradients and reaction rates from particle distribu-
1143 tions. *Journal of Contaminant Hydrology* 120, 99–114.
- 1144 [45] Gillespie, D. T., 1977. Exact stochastic simulation of coupled chemical
1145 reactions. *J. Phys. Chem.* 81 (25), 2340–2361.
- 1146 [46] Gillespie, D. T., 2000. The chemical Langevin equation. *J. Chem. Phys.*
1147 113 (1), 297–306.
- 1148 [47] Gramling, C., Harvey, C., Meigs, L., JUN 1 2002. Reactive transport
1149 in porous media: A comparison of model prediction with laboratory
1150 visualization. *Environmental Science & Technology* 36 (11), 2508–2514.
- 1151 [48] Hammond, G. E., Lichtner, P. C., Sep. 2010. Field-scale model for the
1152 natural attenuation of uranium at the Hanford 300 area using high-
1153 performance computing. *Water Resour. Res.* 46 (9), W09527.
1154 URL <http://dx.doi.org/10.1029/2009WR008819>
- 1155 [49] Hansen, S. K., Scher, H., Berkowitz, B., Jul. 2014. First-principles
1156 derivation of reactive transport modeling parameters for particle track-
1157 ing and pde approaches. *Advances in Water Resources* 69 (0), 146–158.
- 1158 [50] Henshaw, W. D., Schwendeman, D. W., Nov. 2003. An adaptive
1159 numerical scheme for high-speed reactive flow on overlapping grids.
1160 *Journal of Computational Physics* 191 (2), 420–447.
1161 URL <http://www.sciencedirect.com/science/article/pii/S0021999103003231>
- 1162 [51] Herrera, P. A., Valocchi, A. J., Beckie, R. D., Jul. 2010. A multidimen-
1163 sional streamline-based method to simulate reactive solute transport
1164 in heterogeneous porous media. *Advances in Water Resources* 33 (7),
1165 711–727.
1166 URL <http://www.sciencedirect.com/science/article/pii/S0309170810000424>
- 1167 [52] Hills, R. G., Fisher, K. A., Kirkland, M. R., Wierenga, P. J., 1994.
1168 Application of flux-corrected transport to the las cruces trench site.

- 1169 Water Resources Research 30 (8), 2377–2385.
1170 URL <http://dx.doi.org/10.1029/94WR01216>
- 1171 [53] Huang, C.-S., Xiao, F., Arbogast, T., 2015. Fifth order multi-moment
1172 weno schemes for hyperbolic conservation laws. *J. Sci. Comput.* 64,
1173 477–507.
- 1174 [54] Isaacson, S. A., 2013. A convergent reaction-diffusion master equation.
1175 *The Journal of Chemical Physics* 139 (5), 054101.
1176 URL <http://scitation.aip.org/content/aip/journal/jcp/139/5/10.1063/1.4816377>
- 1177 [55] Johnson, J. W., Nitao, J. J., Knauss, K. G., 2004. Reactive transport
1178 modelling of co2 storage in saline aquifers to elucidate fundamental pro-
1179 cesses, trapping mechanisms and sequestration partitioning. Geological
1180 Society, London, Special Publications 233 (1), 107–128.
- 1181 [56] Keating, E. H., Hakala, J. A., Viswanathan, H., Carey, J. W., Pawar,
1182 R., Guthrie, G. D., Fessenden-Rahn, J., 2013. CO₂ leakage impacts
1183 on shallow groundwater: Field-scale reactive-transport simulations
1184 informed by observations at a natural analog site. *Applied Geochem-*
1185 *istry* 30, 136 – 147, *geochemical Aspects of Geologic Carbon Storage*.
1186 URL <http://www.sciencedirect.com/science/article/pii/S0883292712002223>
- 1187 [57] Ketcheson, D. I., Parsani, M., LeVeQue, R. J., 2013. High-order wave
1188 propagations algorithms for hyperbolic systems. *SIAM J. SCI. COM-*
1189 *PUT.* 35 (1), A351–A377.
- 1190 [58] Koch, J., Nowak, W., 2014. A method for implementing dirichlet
1191 and third-type boundary conditions in PTRW simulations. *Water Re-*
1192 *sources Research* 50 (2), 1374–1395.
1193 URL <http://dx.doi.org/10.1002/2013WR013796>
- 1194 [59] Kuzmin, D., 2010. *A Guide to Numerical Methods for Transport Equa-*
1195 *tions*. Friedrich-Alexander-Universität Erlangen-Nürnberg.
- 1196 [60] Labolle, E. M., Fogg, G. E., Tompson, A. F. B., 1996. Random-walk
1197 simulation of transport in heterogeneous porous media: Local mass-
1198 conservation problem and implementation methods. *Water Resour.*
1199 *Res.* 32 (3), 583–593.

- 1200 [61] Le Borgne, T., Dentz, M., Bolster, D., Carrera, J., de Dreuzy, J.-R.,
1201 Bour, O., 2011. Persistence of incomplete mixing: A key to anomalous
1202 transport. *Phys. Rev. E* 84,, 015301(R).
- 1203 [62] Le Borgne, T., Dentz, M., Bolster, D., Carrera, J., De Dreuzy, J.-R.,
1204 Davy, P., 2010. Non-Fickian mixing: Temporal evolution of the scalar
1205 dissipation rate in heterogeneous porous media. *Advances in Water*
1206 *Resources* 33 (12), 1468–1475.
- 1207 [63] Le Borgne, T., Dentz, M., Villermaux, E., 2013. Stretching, coales-
1208 cence, and mixing in porous media. *Physical Review Letters* 110 (20),
1209 204501.
- 1210 [64] Le Borgne, T., Ginn, T. R., Dentz, M., 2014. Impact of fluid defor-
1211 mation on mixing-induced chemical reactions in heterogeneous flows.
1212 *Geophysical Research Letters* 41 (22), 7898–7906.
1213 URL <http://dx.doi.org/10.1002/2014GL062038>
- 1214 [65] Leonard, B., Jun. 1991. The ultimate conservative difference scheme
1215 applied to unsteady one-dimensional advection. *Computer Methods in*
1216 *Applied Mechanics and Engineering* 88 (1), 17–74.
1217 URL <http://www.sciencedirect.com/science/article/pii/004578259190232U>
- 1218 [66] LeVeque, R. J., 1992. *Numerical Methods for Conservation Laws*, 2nd
1219 Edition. Lectures in Mathematics, ETH Zurich. Birkhauser Verlag.
- 1220 [67] LeVeque, R. J., 2002. *Finite Volume Methods for Hyperbolic Problems*.
1221 Cambridge University Press.
- 1222 [68] LeVeque, R. J., 2005. *Numerical Methods for Conservation Laws*, 2nd
1223 Edition. Birkhäuser.
- 1224 [69] Lichtner, P. C., Hammond, G. E., Lu, C., Karra, S., Bisht, G., Andre,
1225 B., Mills, R. T., Kumar, J., 2013. PFLOTRAN user manual. Tech. rep.
- 1226 [70] Lv, Y., Ihme, M., 2014. Discontinuous Galerkin method for mul-
1227 ticomponent chemically reacting flows and combustion. *Journal of*
1228 *Computational Physics* 270, 105 – 137.
1229 URL <http://www.sciencedirect.com/science/article/pii/S0021999114002101>

- 1230 [71] Maier, U., Bürger, C. M., 2013. An accurate method for transient par-
1231 ticle tracking. *Water Resources Research* 49 (5), 3059–3063.
1232 URL <http://dx.doi.org/10.1002/wrcr.20236>
- 1233 [72] Mansell, R. S., Ma, L., Ahuja, L. R., Bloom, S. A., 2002. Adaptive grid
1234 refinement in numerical models for water flow and chemical transport
1235 in soil florida agricultural exp. stn. journal series no. r-08979. 1.
1236 URL <http://dx.doi.org/10.2136/vzj2002.2220>
- 1237 [73] Navarre-Sitchler, A. K., Maxwell, R. M., Siirila, E. R., Hammond,
1238 G. E., Lichtner, P. C., 2013. Elucidating geochemical response of shal-
1239 low heterogeneous aquifers to {CO₂} leakage using high-performance
1240 computing: Implications for monitoring of {CO₂} sequestration.
1241 *Advances in Water Resources* 53, 45 – 55.
1242 URL <http://www.sciencedirect.com/science/article/pii/S0309170812002679>
- 1243 [74] Nitao, J. J., June 2000. Reference Manual for the NUFT Flow and
1244 Transport Code, Version 3.0. Lawrence Livermore National Laboratory.
- 1245 [75] Oldenburg, C. M., Lewicki, J. L., Dobeck, L., Spangler, L., 2009. Mod-
1246 eling gas transport in the shallow subsurface during the zert co2 release
1247 test. *Transport in Porous Media* 82 (1), 77–92.
1248 URL <http://dx.doi.org/10.1007/s11242-009-9361-x>
- 1249 [76] Paster, A., Bolster, D., Benson, D. A., 2013. Particle tracking and the
1250 diffusion-reaction equation. *Water Resour. Res.* 49, 1–6.
- 1251 [77] Paster, A., Bolster, D., Benson, D. A., Apr. 2014. Connecting the
1252 dots: Semi-analytical and random walk numerical solutions of the
1253 diffusion–reaction equation with stochastic initial conditions. *Journal*
1254 *of Computational Physics* 263 (0), 91–112.
1255 URL <http://www.sciencedirect.com/science/article/pii/S0021999114000473>
- 1256 [78] Pedretti, D., Fernández-García, D., Sep. 2013. An automatic locally-
1257 adaptive method to estimate heavily-tailed breakthrough curves from
1258 particle distributions. *Advances in Water Resources* 59 (0), 52–65.
1259 URL <http://www.sciencedirect.com/science/article/pii/S0309170813000869>
- 1260 [79] Pollock, D. W., 1988. Semianalytical computation of path lines for
1261 finite-difference models. *Ground Water* 26 (6), 743–750.
1262 URL <http://dx.doi.org/10.1111/j.1745-6584.1988.tb00425.x>

- 1263 [80] Porta, G., Ceriotti, G., Thovert, J.-F., 2016. Comparative assessment
1264 of continuum-scale models of bimolecular reactive transport in porous
1265 media under pre-asymptotic conditions. *Journal of Contaminant*
1266 *Hydrology* 185–186, 1 – 13.
1267 URL <http://www.sciencedirect.com/science/article/pii/S0169772215300474>
- 1268 [81] Prommer, H., August 2006. PHT3D: A Reactive Multicomponent
1269 Transport Model for Saturated Porous Media. <http://www.pht3d.org>.
- 1270 [82] Prommer, H., Barry, D., Davis, G., 2002. Modelling of physical and
1271 reactive processes during biodegradation of a hydrocarbon plume
1272 under transient groundwater flow conditions. *Journal of Contaminant*
1273 *Hydrology* 59 (1–2), 113 – 131, the 2000 Contaminated Site Remediation
1274 Conference: From Source Zones to Ecosystems.
1275 URL <http://www.sciencedirect.com/science/article/pii/S0169772202000785>
- 1276 [83] Roe, P. L., Baines, M. J., 1982. Algorithms for advection and shock
1277 problems. In: Viviand, H. (Ed.), *Proc. 4th GAMM conference on Numerical*
1278 *Methods in Fluid Mechanics*.
- 1279 [84] Salamon, P., Fernández-Garcia, D., Gómez-Hernández, J. J., 2006.
1280 Modeling mass transfer processes using random walk particle tracking.
1281 *Water Resour. Res.* 42 (11), W11417–.
1282 URL <http://dx.doi.org/10.1029/2006WR004927>
- 1283 [85] Salamon, P., Fernández-Garcia, D., Gómez-Hernández, J. J., 2006. A
1284 review and numerical assessment of the random walk particle tracking
1285 method. *Journal of Contaminant Hydrology* 87 (3–4), 277 – 305.
1286 URL <http://www.sciencedirect.com/science/article/pii/S0169772206000957>
- 1287 [86] Sanchez-Vila, X., Dentz, M., Donado, L. D., 2007. Transport-controlled
1288 reaction rates under local non-equilibrium conditions. *Geophysical Research*
1289 *Letters* 34 (10).
- 1290 [87] Sanchez-Vila, X., Fernández-Garcia, D., Guadagnini, A., 2010. Inter-
1291 pretation of column experiments of transport of solutes undergoing
1292 an irreversible bimolecular reaction using a continuum approximation.
1293 *Water Resources Research* 46 (12).
- 1294 [88] Schwede, R. L., Cirpka, O. A., Nowak, W., Neuweiler, I., 2008. Impact
1295 of sampling volume on the probability density function of steady state

- 1296 concentration. *Water Resources Research* 44 (12), W12433, w12433.
1297 URL <http://dx.doi.org/10.1029/2007WR006668>
- 1298 [89] Smolarkiewicz, P. K., 1984. A fully multidimensional positive definite
1299 advection transport algorithm with small implicit diffusion. *Journal of*
1300 *Computational Physics* 54 (2), 325 – 362.
1301 URL <http://www.sciencedirect.com/science/article/pii/0021999184901219>
- 1302 [90] Steefel, C. I., October 2009. CrunchFlow Software for Modeling Mul-
1303 ticomponent Reactive Flow and Transport CrunchFlow CRUNCH-
1304 FLOW, Software for Modeling Multicomponent Reactive Flow and
1305 Transport, USER’S MANUAL. Earth Sciences Division, Lawrence
1306 Berkeley National Laboratory, Berkeley, CA 94720 USA.
- 1307 [91] Steefel, C. I., Appelo, C. A. J., Arora, B., Jacques, D., Kalbacher, T.,
1308 Kolditz, O., Lagneau, V., Lichtner, P. C., Mayer, K. U., Meeussen, J.
1309 C. L., Molins, S., Moulton, D., Shao, H., Šimůnek, J., Spycher, N.,
1310 Yabusaki, S. B., Yeh, G. T., 2014. Reactive transport codes for sub-
1311 surface environmental simulation. *Computational Geosciences* 19 (3),
1312 445–478.
1313 URL <http://dx.doi.org/10.1007/s10596-014-9443-x>
- 1314 [92] Sweby, P. K., Oct. 1984. High resolution schemes using flux limiters
1315 for hyperbolic conservation laws. *SIAM Journal on Numerical Analysis*
1316 21 (5), 995–1011.
1317 URL <http://www.jstor.org/stable/2156939>
- 1318 [93] Tambue, A., Lord, G., Geiger, S., May 2010. An exponential integrator
1319 for advection-dominated reactive transport in heterogeneous porous
1320 media. *Journal of Computational Physics* 229 (10), 3957–3969.
1321 URL <http://www.sciencedirect.com/science/article/pii/S0021999110000604>
- 1322 [94] Tartakovsky, A. M., Meakin, P., Scheibe, T. D., Eichler West,
1323 R. M., 2007. Simulations of reactive transport and precipitation with
1324 smoothed particle hydrodynamics. *Journal of Computational Physics*
1325 222 (2), 654–672.
- 1326 [95] Tartakovsky, A. M., Tartakovsky, D. M., Scheibe, T. D., Meakin, P.,
1327 2008. Hybrid simulations of reaction-diffusion systems in porous media.
1328 *SIAM Journal on Scientific Computing* 30 (6), 2799–2816.

- 1329 [96] Thuburn, J., 1996. Multidimensional flux-limited advection schemes.
1330 Journal of Computational Physics 123 (1), 74 – 83.
1331 URL <http://www.sciencedirect.com/science/article/pii/S0021999196900066>
- 1332 [97] Tompson, A., Dougherty, D., JUL 1992. Particle-grid methods for re-
1333 acting flows in porous-media with application to Fisher equation. Appl.
1334 Math. Model. 16 (7), 374–383.
- 1335 [98] Toro, E. F., 2009. Riemann Solvers and Numerical Methods for Fluid
1336 Dynamics, A Practical Introduction (3rd edition). Springer.
- 1337 [99] Van Dyke, M., 1975. Perturbation Methods in Fluid Mechanics.
1338 Parabolic Press, Stanford.
- 1339 [100] van Leer, B., 1974. Towards the ultimate conservative difference
1340 scheme. ii. Monotonicity and conservation combined in a second-order
1341 scheme. J. Comput. Phys. 14, 361–370.
- 1342 [101] van Zon, J. S., ten Wolde, P. R., Apr. 2005. Simulating biochemical
1343 networks at the particle level and in time and space: Green’s function
1344 reaction dynamics. Phys. Rev. Lett. 94 (12), 128103–.
- 1345 [102] von Smoluchowski, M., 1917. Versuch einer mathematischen theorie der
1346 koagulationskinetik kolloider lösungen. Z. Phys. Chem 92, 124–168.
- 1347 [103] Werth, C. J., Cirpka, O. A., Grathwohl, P., 2006. Enhanced mixing and
1348 reaction through flow focusing in heterogeneous porous media. Water
1349 Resources Research 42 (12), W12414, w12414.
1350 URL <http://dx.doi.org/10.1029/2005WR004511>
- 1351 [104] White, M., Oostrom, M., October 1997. STOMP, Subsurface Transport
1352 Over Multiple Phases. Pacific Northwest National Laboratory, Rich-
1353 land, WA, report pnnl-11218 Edition.
- 1354 [105] Wolfsberg, A. V., Freyberg, D. L., 1994. Efficient simulation of single
1355 species and multispecies transport in groundwater with local adaptive
1356 grid refinement. Water Resources Research 30 (11), 2979–2991.
1357 URL <http://dx.doi.org/10.1029/93WR02749>

- 1358 [106] Xu, T., Sonnenthal, E., Spycher, N., Zheng, L., June 2014.
1359 TOUGHREACT V3.0-OMP Reference Manual: A Parallel Simula-
1360 tion Program for Non-Isothermal TOUGHREACT V3.0-OMP Ref-
1361 erence Manual: A Parallel Simulation Program for Non-Isothermal
1362 Multiphase Geochemical Reactive Transport. Earth Sciences Divi-
1363 sion, Lawrence Berkeley National Laboratory University of California,
1364 Berkeley, CA 94720, draft Edition.
- 1365 [107] Yeh, G.-T., Sun, J., Jardine, P. M., Burgos, W. D., Fang, Y., Li,
1366 M.-H., Siegel, M. D., May 2004. HYDROGEOCHEM 5.0: A Three-
1367 Dimensional Model of Coupled Fluid Flow, Thermal Transport, and
1368 HYDROGEOCHEMical Transport through Variably Saturated Con-
1369 ditions: Version 5.0. OAK RIDGE NATIONAL LABORATORY.
- 1370 [108] Zhang, Y., Benson, D. A., Meerschaert, M. M., LaBolle, E. M., Schef-
1371 fler, H.-P., AUG 2006. Random walk approximation of fractional-order
1372 multiscaling anomalous diffusion. Phys. Rev. E 74 (2, Part 2).
- 1373 [109] Zheng, C., Wang, P. P., 1999. MT3DMS: A Modular Three-
1374 Dimensional Multispecies Transport Model for simulation of advection,
1375 dispersion and chemical reactions of contaminants in groundwater sys-
1376 tems; documentation and user's guide. U.S. Army Engineer Research
1377 and Development Center, Vicksburg, MS, contract report serdp-99-1
1378 Edition.
- 1379 [110] Zyvoloski, G., 1997. Summary of the Models and Methods for the
1380 FEHM Application – A Finite-Element Heat- and Mass-Transfer Code.
1381 Los Alamos National Laboratory Tables, Los Alamos, NM 87545,
1382 United States.